Design of an Omnidirectional Soft Tactile Sensor with Applications in Leak Detection

by

Tyler Takeo Okamoto

Submitted to the Department of Mechanical Engineering
in partial fulfillment of the requirements for the degree of

Master of Science in Mechanical Engineering

at the

MASSACHUSETTS INSTITUTE OF TECHNOLOGY

June 2019

Author..... Signature redacted .....
Department of Mechanical Engineering
May 10, 2019

Certified by..... Signature redacted .....
Kamal Youcef-Toumi
Professor, Department of Mechanical Engineering
Thesis Supervisor

Signature redacted

Accepted by..... .....
Nicolas Hadjiconstantinou
Chairman, Committee on Graduate Students

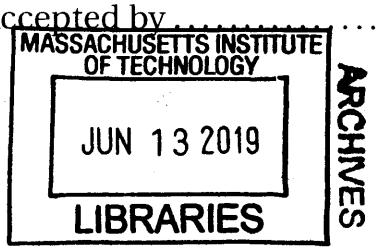

Design of an Omnidirectional Soft Tactile Sensor with Applications in Leak Detection

by

Tyler Takeo Okamoto

Submitted to the Department of Mechanical Engineering
on May 10, 2019, in partial fulfillment of the
requirements for the degree of
Master of Science in Mechanical Engineering

Abstract

Soft robots have many unique geometries requiring different tactile feedback mechanisms. In order to respond to their environment, soft robots would benefit by having multi-axis sensors that can determine how a surface is being contacted. As a particular application, previous soft sensor designs are used to detect leaks in active water pipes, but have difficulty differentiating leaks from pipe joints and obstacles.

This thesis presents the design, fabrication and experimental testing of soft, multi-axis deformation sensors. In the first approach, various geometries of a piezoresistive rubber sensor were tested, and the soft-bodied drone for mapping the interior of pipes was demonstrated in a field test conducted in Matão, Brazil. This demo yielded some design realizations, which led to changes in the sensing technology in order to provide more detail about the interior pipe features. Thus, highly flexible conductive fabric and silicone capacitors were investigated as the capacitance sensing element, which exhibits linearity, faster response time, and less hysteresis. Multiple copies of this sensor were arranged in a particular way to decouple the four deformation modes of the material: uniaxial tension, bending, compressive pressure, and torsion. Furthermore, this sensor is well-suited for the detection of leaks, obstacles, and pipe joints in active water pipes.

Thesis Supervisor: Kamal Youcef-Toumi
Title: Professor, Department of Mechanical Engineering

Acknowledgments

I would like to thank Dr. Kamal Youcef-Toumi for providing advice and resources for the project. He has helped me grow as a researcher, and has given me the opportunity to try many different approaches and learn from each project. I would also like to thank Jiyoung Chang for helping with the design and testing of the capacitive sensors. Furthermore, I would like to thank MathEarth Inc. (f.k.a. Banxin Corporation) for continued financial support of the leak detection and repair project, meeting with us to discuss details, and providing their water pipe test facility. I also want to thank my labmates Steven Yeung, Xiaotong Zhang, and Elizabeth Mittmann for advancing the in-pipe leak detection and repair robots in the Mechatronics Research Laboratory, and making the Brazil field test possible. Finally, my work was helped by the Impact and Crashworthiness Lab at MIT for allowing use of their Instron test equipment, MIT Makerworks and the MIT Hobby Shop for access to fabrication equipment, the MIT Bioinstrumentation lab for use of their SEM, and Dr. Simona Socrate and Dr. David Parks for meeting to discuss the strengths and limitations of the mechanical design of the capacitive sensors.

Contents

List of Figures

List of Tables

Chapter 1

Introduction

1.1 Soft Robotics

Soft robotics enables mechanisms to branch into applications like health monitoring, assistive devices, and biomimicry. Soft robots use soft actuators to interact with the world, and there are many mechanisms that enable this movement, including . In addition to actuators, soft robots need sensors to perceive the world, has a growing need for multi-axis tactile sensing. Flexible soft sensors have the ability to measure bending and surface contact pressure. However, an even more versatile sensor would be able to measure bending, pressure, tension and torsion. Such a sensor could provide insight about the geometry of the object the sensor is interacting with. Furthermore, this type of soft sensor has applications to monitor body movements in wearable devices [1], tactile sensing for robot skin, prehension in anthropomorphic hands, crawling robots, wearable health monitoring devices, and water pipe leak detection.

1.1.1 Soft Actuators

Soft actuators are necessary for locomotion, and depending on the particular environment and length scale, various design strategies may be used. For instance pneumatics can be used to contract or expand a gripper using vacuum to contract the structure via beam buckling, similar to how muscles behave [35]. Since the system is soft, it is able

to reversibly buckle and unbuckle, whereas this deformation in a more rigid material would result in permanent deformation or failure. A system may expand when exposed to light [37], contract by resistive heating in an SMA [36], or using a shape memory alloy to act as a gripper [13]. The light driven robot has very small mass, so surface forces dominate the movement. While novel, its millimeter scale size restricts it from exerting large forces on the environment. The resistive heating approach allows a substrate to curl when the silver wire is heated to angles exceeding 120°, however it takes around 3 min to approach its steady state angle [36]. The gripper using SMA wires presents a useful application of this technology, since it can pick up objects 15 times heavier than the gripper itself, with geometries that are not perfectly radially symmetric [13].

These soft robots all need to be manually controlled via a human-in-the-loop, since they do not have a method to provide feedback to a central controller. This makes soft robot autonomy significanly more challenging. Thus it is also necessary to instrument these soft robots with soft sensors, that are able to measure properties like strain, deformation direction, and force applied.

1.1.2 Soft Sensors

The flexible nature of soft materials makes conventional encoders, metal strain gauges, and IMUs ineffective. Thus, soft robotics depends on highly flexible curvature sensors for sensing [25]. Some curvature sensors rely on a conductive liquid known as eutectic gallium indium (eGaIn), which changes resistance when it enlongates due to curvature [20].

Existing soft sensor transducers include resistive and piezoresistive sensors, magnetic sensors, inductive sensors, and capacitive sensors. Each of these provide unique capabilities and have the potential to provide functionality. Many of these sensors are inspired by biology, and technologies are invented to mimic that of nature. For instance, tactile bleps on a tendril uses a cytoskeleton membrane to create a force sensor and transducer [8], epidermal rays in star-nosed moles have Eimer's organs that form a tactile strucure with over 100,000 myelinated fibers for quick and high resolution sensing [6], and spiders' slit sensilla in the exoskeleton which are able to measure compressive

exoskeletal strains [4]. By deconstructing mechanisms like these, it provides insight into how soft tactile feedback systems may be designed, fabricated, and miniaturized for other applications.

In addition to deriving sensors from biology, sensors may also be used to integrate to biological systems like human skin. For instance, a skin-like optoelectronic system has been demonstrated to characterize the skin in terms of heart rate, tissue oxygenation, and ultraviolet dosimetry, and transmit this data through NFC [15]. This shows that miniature electronics can be embedded into a thin and flexible membrane, and can operate without a battery. In another work, a stretchable ionic touch panel was created that was able to record a single touch in two dimensions, even when the touch panel was stretched or curved around an arm [14]. This demonstrates that hydrogels with dissolved ions are one pathway to achieve a high resolution touch display for one point of contact. While these methods show promise that they are able to localize contact forces and have the flexible properties desired of soft systems, they are not able to characterize bending or tension forces throughout the material.

For this project, the goal was to create an omnidirectional soft sensor that can decouple its bending modes, whether it is subjected to uniaxial tension, bending, torsion, or compressive pressure. There are many types of sensors that are able to characterize loads. However, most have severe limitations that make it difficult to implement in a fully general deformation sensor. For example,

- resistive and piezoresistive sensors exhibit large hysteresis, overshoot, and transient behaviors [1]
- optical sensors have complex fabrication methods and limited maximum strain [30]
- magnetic sensors are prone to interference around ferromagnetic objects [23], [29]
- inductive sensors require complex signal processing and is difficult to miniaturize [9].

In contrast, capacitive sensors show linearity, high sensitivity, quick response times,

and have a large dynamic range [30]. Capacitive sensors using conductive textiles as the electrode have been demonstrated to be sensitive to normal force as well as tangential forces [28]. These fabric sensors have been used to analyze finger motions in a glove [2], [3]. Capacitive sensing can also be achieved through expanded intercalated graphite, fabricated using direct writing of elastomer through extrusion, and screen printing [31]. In addition, soft capacitive sensors for a soft prosthetic hand were constructed using conductive nanocomposite electrodes, and were used to sense both curvature and touch [24], [26]. Even ionic-hydrogel electrodes have been implemented in a pneumatic crawling robot for deformation sensing and tactile feedback [18].

While there are many approaches to capacitance based sensing, the method that showed impressive repeatability, flexibility were the fabric based capacitors. Therefore, capacitance-based fabric and silicone sensors were chosen as the basis for the work presented here.

By arranging an array of capacitive sensors in a particular manner, and bonding it to a silicone sheet, it is possible to measure and decouple four modes of deformation: uniaxial tension, bending, pressure, and torsion. Given the performance characteristics of this device, it is well-suited for underwater systems to monitor the leaks in pipes, and differentiate it from the obstacles and pipe joints that an inspection robot may encounter.

1.2 Leak Detection

1.2.1 Leak Detection Methods

USA municipalities lose 15-25% of its water supply, with most of the losses being attributed to leakages [27]. Current leak sensing technologies typically require the pipe to be dry to be inspected, resulting in the loss of service for the users. This includes robotic inspection [5], in which a tethered mobile system would inspect the pipe using acoustic or optical methods. This method requires a skilled technician to maneuver the robot. There exist other untethered passive devices like the Smartball, which uses acoustic in-

struments to inspect active water pipes without a human operator, but only work in large metal pipes and requires a specialist to interpret the data [16]. Finally, there are out-of-pipe methods that detect leaks via acoustic signals, or by installing leak noise correlators around a suspected leak [12], [11]. However, the acoustic method is slow and requires tracing the pipeline manually, and leak noise correlators are not effective in plastic pipes [21], [22].

1.2.2 Soft Sensors in Leak Detection

Soft sensors offer a way to do in-situ leak detection in active water pipes. One sensing technology involves using piezoresistive rubber to measure the strain of a thin, flexible membrane as it is pulled by a leak [33]. Leaks in a water or gas pipe cause a localized pressure gradient near the interior surface of the leak [7]. This resistive based approach is explored and analyzed within Chapter 2, and validated in a field test in Brazil in section 2.4.

1.2.3 Knowledge Gap

This piezoresistive sensor can detect the presence of a leak, but it has difficulty differentiating leaks from obstacles and other pipe features, resulting in false positives. This is because each sensor only has one scalar output, and leaks and obstacles both pull on the sensor with similar magnitudes. In addition, conductive silicone composite (CSC) sensors have a transient response between 9-13.8% of the steady-state behavior, variance over repeated trials of 2.37-2.48%, a slow time constant of 12-19 seconds, and a hysteresis width of 17-26% [10]. These side effects make it difficult to calculate the forces acting on the sensor, especially when leaks are passed over in under 0.2 seconds. With the CSC sensor, leaks, obstacles, and pipe bends all cause the sensor to respond, so sensor fusion with the accelerometer and gyro is needed to determine if the sensor fluctuation was also coupled with a pipe joint [33]. However, the sensor described in Chapter 3 can differentiate between four deformation modes, so additional sensors are not required.

1.2.4 State of the Art Leak Detection

In Chapter 3, we investigate an array of capacitive based soft fabric sensors. These sensors demonstrate linearity, and can be used to decouple the effects of uniaxial strain, bending, torsion, and pressure. By combining these decoupled signals, it offers a more reliable approach to characterize not only leaks, but also obstacles, pipe joints and bends.

1.3 Thesis Outline

In this thesis, the soft piezoresistive strain sensor is detailed, from the theory to fabrication steps to the testing of the sensors. It was found that modifying the geometry of the rubber sensor had a direct effect on its strain to resistance profile. Next, the piezoresistive sensor and soft bodied pipe inspection drone was fabricated and tested in Brazil in a real-world field test, validating the sensor and soft-bodied drone as a viable pipe inspection tool.

Next, a capacitive based sensor that could decouple bending modes was designed and tested. This capacitive sensor had a particular arrangement of six unit sensor elements such that the group would respond differently to its four primary deformation modes. These are deformation in uniaxial tension, bending, torsion, and compressive pressure. A decoupling methodology was presented using the principle of superposition to calculate the contribution from each bending mode on the resultant capacitance change. By having such a general sensor, it was shown that it would have the potential to make leak detection more robust with more geometric information.

Finally, recommendations are presented to inspire future work and extensions to other fields are proposed.

Chapter 2

Piezoresistive Sensor Design

2.1 Sensor Design

2.1.1 Background Theory

Piezoresistive rubber is used as the sensing element of this soft sensor. The resistance of this rubber changes in response to its strain, and this change in resistance can be measured using a voltage divider circuit. Using a microcontroller, it is possible to measure the voltage drop across the sensor dynamically, and thus calculate its effective resistance.

Piezoresistive rubber has numerous advantages over other compliant sensors. It is cost-effective, can be shaped into various patterns, and has a quick response time.

2.1.2 Methodology

Material Selection

The first type of piezoresistive rubber used in this study is a conductive carbon-black filled rubber, similar to Stockwell Elastomerics SE65-CON rubber with 1.0mm thicknesss (Table A.2). This material can be stretched up to 100% strain and has a two-phase resistance-strain relationship. When the rubber is stretched between 0-25% strain the resistance increases. This effect is due to the rubber being incompressible, so when the

substrate is stretched, the beads inside grow farther apart from each other, increasing the resistance. However, with strains between 25-100%, the beads actually get compressed together as a result of the thickness of the substrate decreasing significantly.

The second type of piezoresistive rubber is Zoflex CD45.1 with 1.0mm thickness (Table A.2). It is a gray material with limited stretchability. Its resistance increases monotonically when stretched, and becomes non-conductive when stretched close to failure. As shown in Figure 2-1, the microstructure is composed of many beads that are fused together. In the unstretched configuration, the beads overlap and have low resistance. When the material is stretched, the overlap area decreases, which results in a much greater effective resistance.

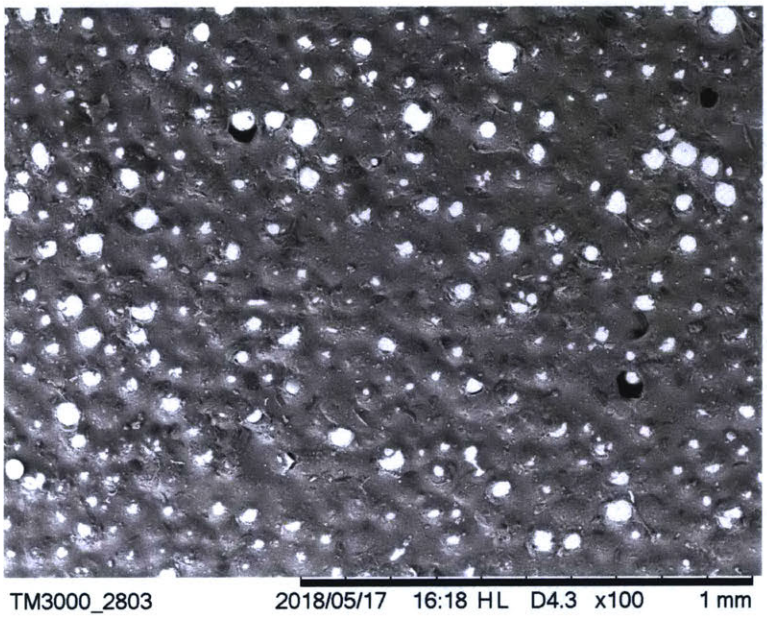

Figure 2-1: SEM Image of Zoflex CD45.1 Microstructure. Image was taken with the help of the MIT Bioinstrumentation Lab.

Geometric Patterns

The sensitivity of the sensor is highly dependent on the geometry. Due to the sensor's nonlinear behavior, different geometries can cause the sensor to operate in different regimes. In the rectangular strip test, the resistance decreased with increasing tension. However, for the spiral strip sensor subject to radial tension, it was found that applying this radial load caused the resistance to increase at first, and when a threshold is passed,

the resistance decreases. In Figure 2-2, two geometric models are shown which have different behaviors when a force is applied.

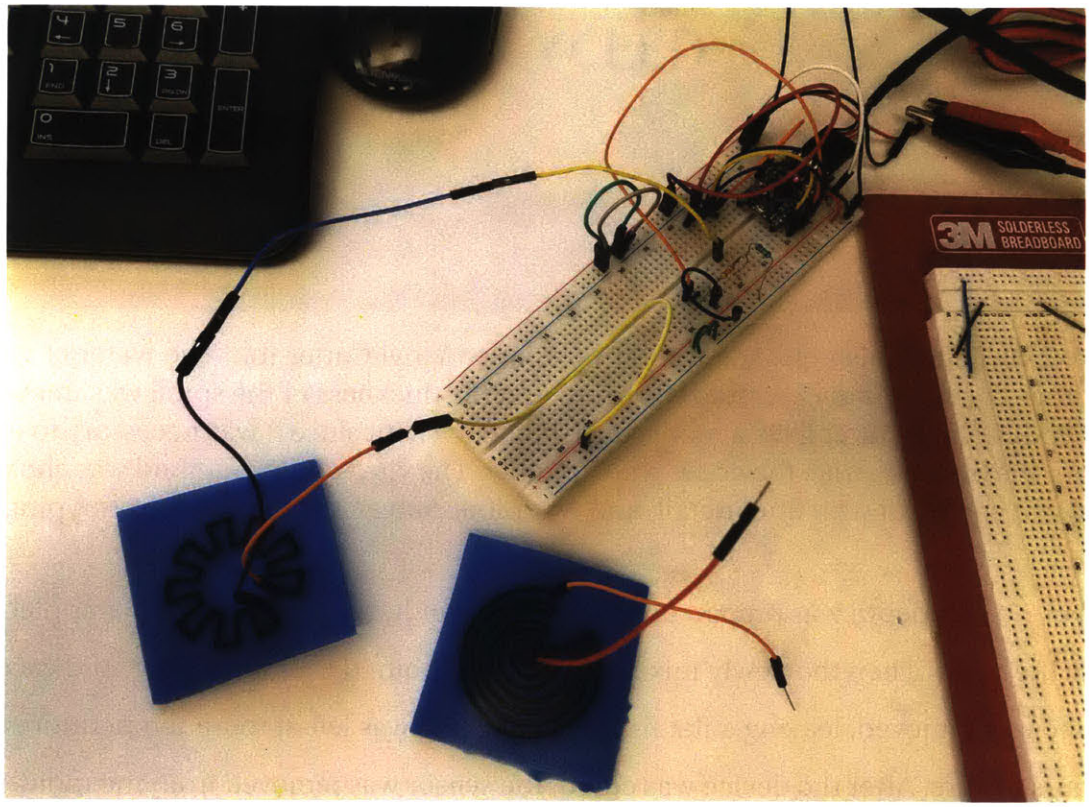

Figure 2-2: Two geometric molds for resistive-based force characterization

Fabrication

In order to fabricate these sensors, a sheet of carbon-black infused conductive rubber of 1.0 mm thickness is used as the sensing element. This sheet is placed onto a semi-sticky plastic mat for vinyl cutting, and is loaded into a Cameo Silhouette vinyl cutter with the "Stamp Material" setting (Table A.3). The desired geometry is loaded into the vinyl cutter, and the sensor is cut accordingly. Most times the rubber will only be cut 80% of the way, so the rest of the sensor needs to be pulled apart by hand. The edge finish can be seen in Figure 2-3.b.

For the bulk elastomer, Mold Star 30 from Smooth-On, Inc. was used (Table A.2). Two equal volumes of Part A and Part B of the Mold Star 30 were mixed together and a vacuum chamber was used to remove air bubbles trapped by the mixing process. A 3D printed

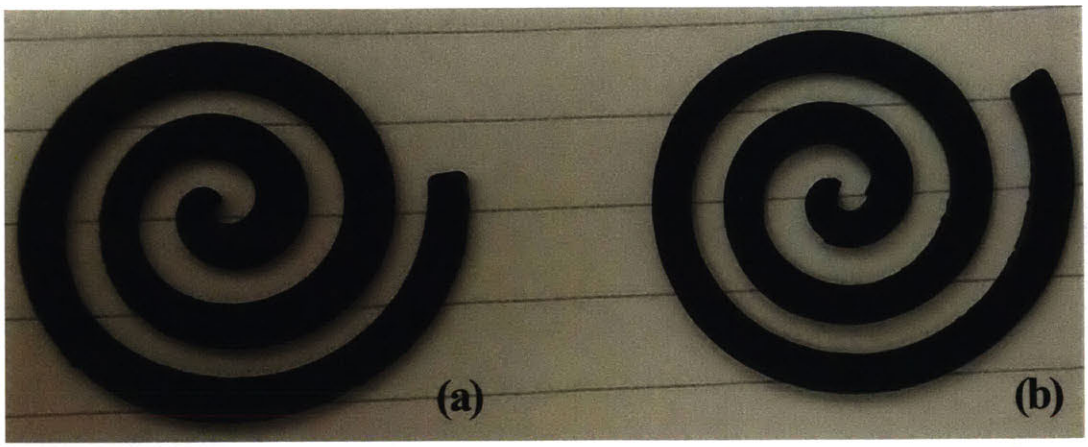

Figure 2-3: Edge Finish on Waterjet (a) vs. Cameo Vinyl Cutter (b). The waterjet gave smoother contours, but oversized the print, and the thickness of the spiral was uneven. The CAMEO vinyl cutter gave a more consistent curve, but since it was necessary to tear it out of the bulk material, the edges were rougher. The vinyl cutting method was chosen because it could cut with finer detail, and was more convenient for rapid prototyping.

mold of 2.0 mm depth was prepared, and a precut conductive rubber sensor was placed inside the mold. Then the newly mixed silicone was poured over the sensor, and excess silicone was removed, leaving a flat finish. The sensor was left at room temperature for 24 hours to cure. After the device was cured, the sensor was removed from the mold.

To measure the effective resistance of the rubber, jumper wires were used to pierce both ends of the rubber sensor, and both leads were attached to a resistance measuring circuit, as detailed in the next section.

2.2 Sensor Testing

2.2.1 Resistance Measuring Circuit

In order to measure the resistance of the sensor accurately over time, a voltage divider circuit was used, as shown in Figure 2-4. It is composed of the voltage divider with the variable resistance sensor in series with a fixed resistor. To maximize sensitivity, the resistor chosen is the geometric mean of the maximum and minimum expected resistance of the variable resistor. For this experiment, the resistance varied between 500kΩ and 2.5MΩ, so a resistor of 1.2MΩ was chosen.

$$R_2 = \sqrt{R_{min} R_{max}} \tag{2.1}$$

An unity gain op-amp buffer was used to probe the voltage between the fixed resistor and the sensor, while minimizing current draw as shown in Figure 2-4. This is followed by a low-pass filter to reduce signal noise. A resistor-capacitor pair was chosen to create a low-pass filter with cutoff frequency 15.6 Hz. This cutoff was chosen to be just faster than the expected time constant of a signal from a leak (0.2s), and is slower than the high-frequency noise (60 Hz and higher) that obfuscates the desired signal. This would allow measuring signals as fast as 8 Hz while dampening high frequency noise in the system. Finally, a NI myDAQ was used to record the raw voltage signals from the voltage divider and the force cell at 263 Hz (Table A.4).

$$f_c = \frac{1}{2\pi RC} = \frac{1}{2\pi(10 \times 10^3)(1.0 \times 10^{-6})} = 15.6Hz \tag{2.2}$$

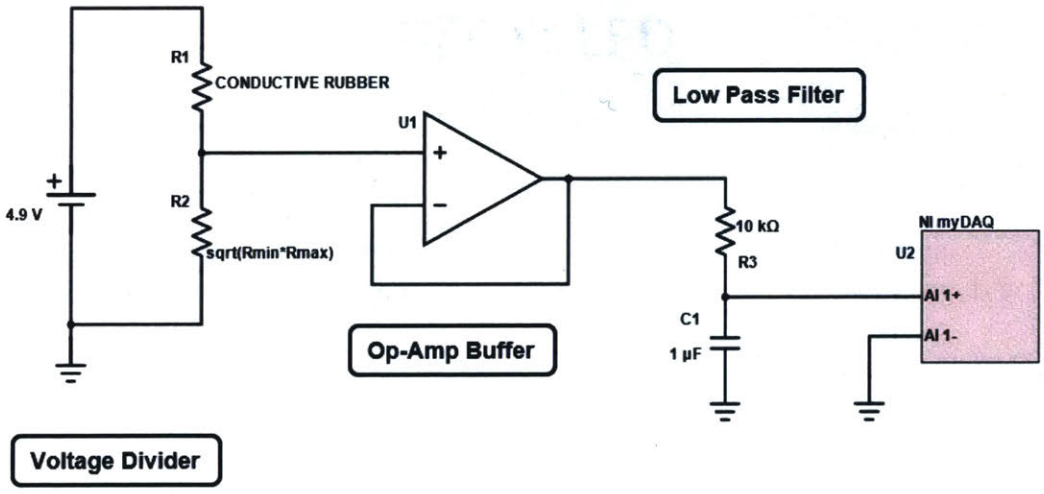

Figure 2-4: Schematic for resistance measuring circuit

2.2.2 Labview Code

Figure 2-5 shows the frontend interface used to track the resistance of the sensor over time. In 2-5.a, there is a drop-down to select the serial COM port, and a text box to enter the shunt resistor value in the voltage divider circuit. 2-5.b is a live indicator that

shows the raw voltage value, the waveform charts on the right shows the raw voltage in the range 0-5 V, with a short time history (2-5.c) and a longer time history (2-5.e). 2-5.d shows the converted resistance value based on the shunt resistor used in the circuit. When the sensor is stretched, the resistance increases sharply from 500 kΩ to 3 MΩ. Finally 2-5.f shows the raw voltage coming out of the force cell. Together, all these graphs enable quick testing of new sensor designs and sensitivity analysis.

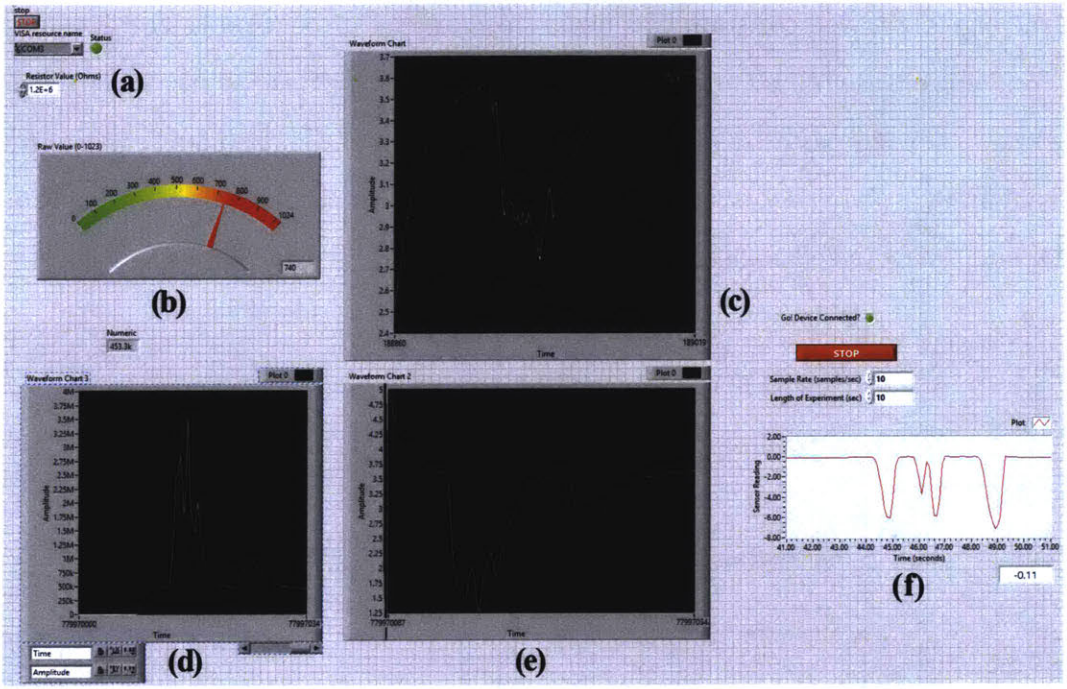

Figure 2-5: Labview Frontend Interface. This setup enables rapid testing of sensors by allowing the dynamic resistance change of various sensors to be recorded and visualized.

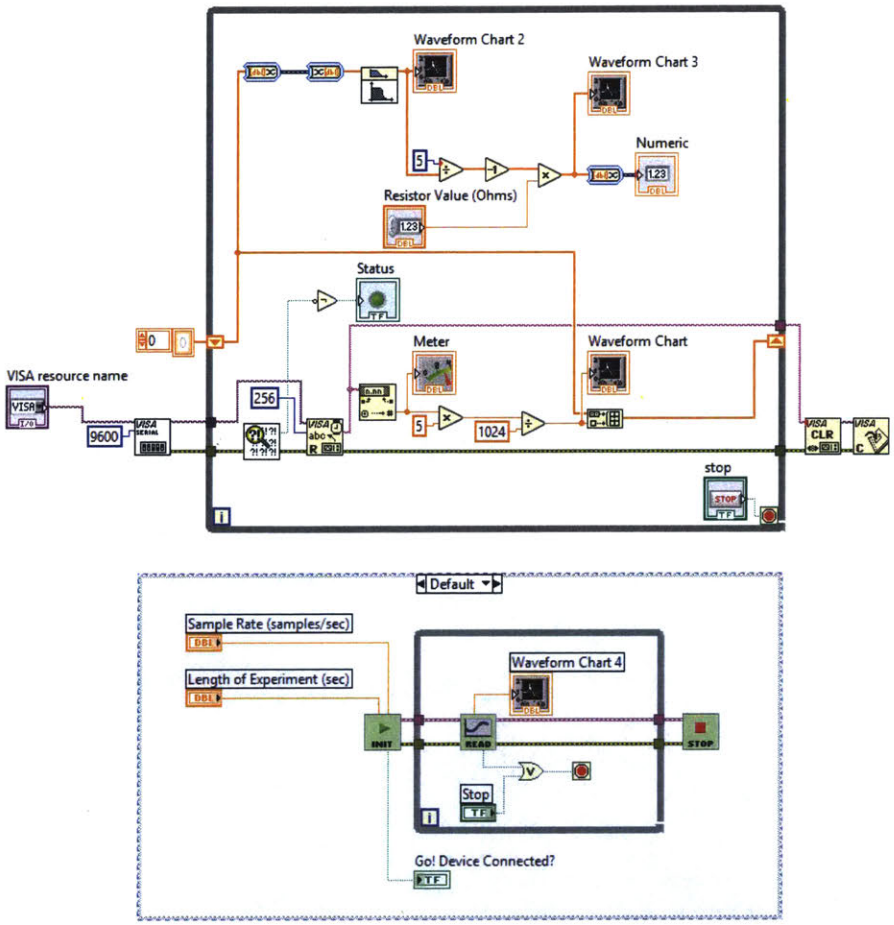

Figure 2-6: This Labview script allows real time resistance data to be collected and plotted on a graph. An arduino is used to collect the raw voltage data in the voltage divider circuit, and then circuit analysis is used to convert the signal to an effective resistance of the sensor. Both the voltage and resistance are plotted on a waveform graph, as well as a live dial indicator for quick visual diagnosis. Different shunt resistors can be used in the voltage divider circuit to match the sensitivity range of the sensor, and this resistor value can be inputted into the interface.

2.2.3 Uniaxial Tension

Since the piezoresistive rubber has a mode that increases resistance in the first phase, and then starts to decrease in resistance.

Carbon Black Filled Rubber

In this test, a vertical strip of carbon black filled rubber was embedded in a square substrate made of the blue Mold Star 30 rubber. The bottom of the sample was clamped and fixed, while the top of the sample was clamped and attached to a Vernier Dual-range 10N/50N load cell. A NI MyDAQ was used to collect data from the load cell and the voltage divider circuit simultaneously. Next, the top of the sensor was pulled via the load cell until a force of 9 N was obtained, it was held for 3 seconds, and then the tension was slowly released. The resulting resistance-force relationship is plotted in Figure 2-7.

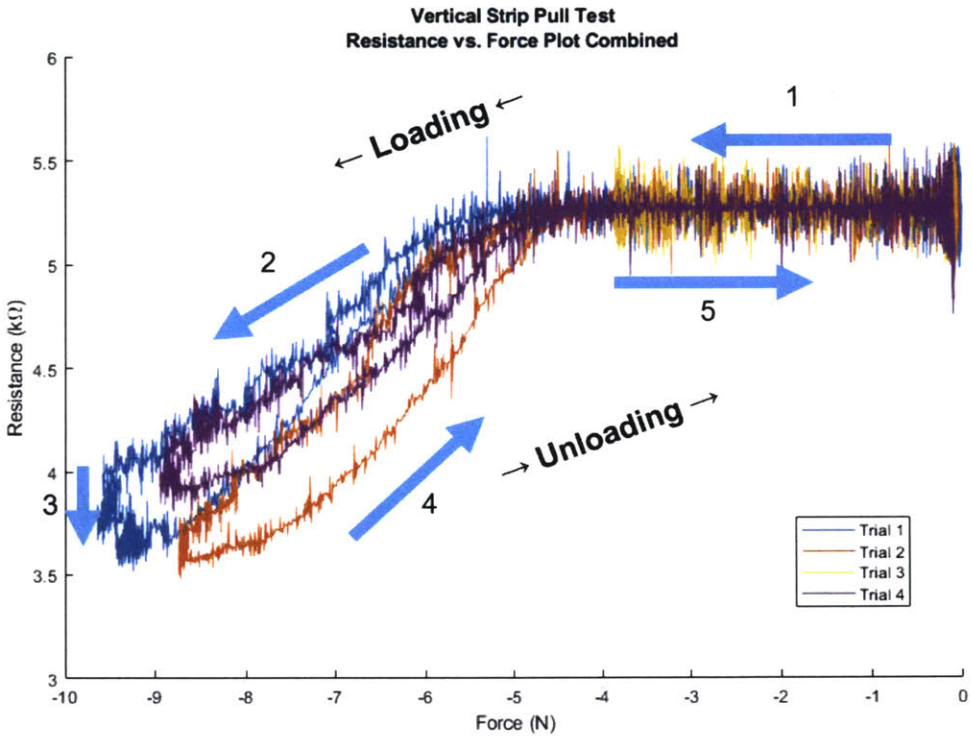

Figure 2-7: Vertical strip test

Figure 2-7 has five distinct sections labeled with blue arrows. All four trials had similar responses, however the maximum force varied between 8.7-9.6 N. Forces are shown as negative values because in this experiment, compression was defined as positive.

1. The weight of the system pulls on the force cell without deforming the rubber

2. The resistance decreases almost linearly as force increases

3. When the force is held constant for 3 seconds, the resistance continues to drop, approaching a steady state value

4. When the load is relieved, the resistance returns to the original value with no overshoot

5. The resistance is constant with no load applied

This shows that when there is no slack in the sensor, there is a roughly linear relationship between the amount of load and the resulting resistance. However, as shown in section 3, there is some drift over time as the resistance value settles to its steady-state stretched behavior. This may be due to the viscoelastic properties of the rubber, taking some time to distribute internal stresses. In addition, the return path follows a different shape from the forward path, indicative of hysteresis within the sensor's response. This makes it more difficult to perform the inverse calculation using the resistance value to calculate the force applied.

2.2.4 Radial Tension

In this test, a spiral strip of carbon black filled rubber was embedded inside a 2.5 mm thick square mold. The sensor is placed in a fixture that clamps around the circular spiral sensor, leaving the center exposed, as shown in Figure 2-8. A hemispherical tip is affixed to the end of the Vernier Dual-Range Force Sensor, which is attached to a Dremel test stand. The test stand is lowered slowly, pressing on the center of the spiral membrane, held for 3 seconds, and then released slowly.

It was found that there was a two-phase relationship in the force to resistance graph. If the load is less than 0.2 N, the resistance increases as the force increases. This is because the sensor is in the incompressible regime, where the carbon black particles spread out when the material is subject to small displacements [17]. However, at 0.2 N, the behavior changes abruptly, and the resistance starts to decrease drastically when more load is applied. This is explained with the compressible model, in which the conductive particles are compressed together (increasing conduction) as the cross-sectional area of the material decreases [17].

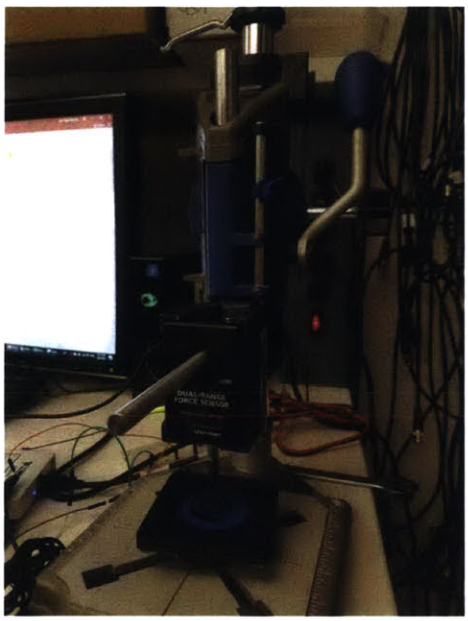

Figure 2-8: Setup for point compression on spiral design. A Dremel stand is used as the test stand. A 3D printed adapter is used to connect the stand to the Vernier Dual-Range Force Sensor, set up to record ±10 N. The tip of the force cell has a hemispherical tip of diameter 0.25". A 3D printed clamp fixes the spiral membrane in place directly below the force sensor, constraining it on its circumference, while leaving space for it to deflect below.

Figure 2-9 has six distinct sections labeled with blue arrows.

1. Between 0-0.2 N, the load increases the resistance of the rubber.

2. From 0.2-2.3 N, the resistance decreases by 50%

3. When the force is held constant for 3 seconds, the resistance continues to drop, approaching a steady state value

4. When the load is relieved, the resistance increases along a lower curve until it reaches 0.2N

5. At 0.2N, there is an inflection point where the material overshoots the original resistance but at a slower rate than the previous section

6. With no load, the material returns to its original resistance

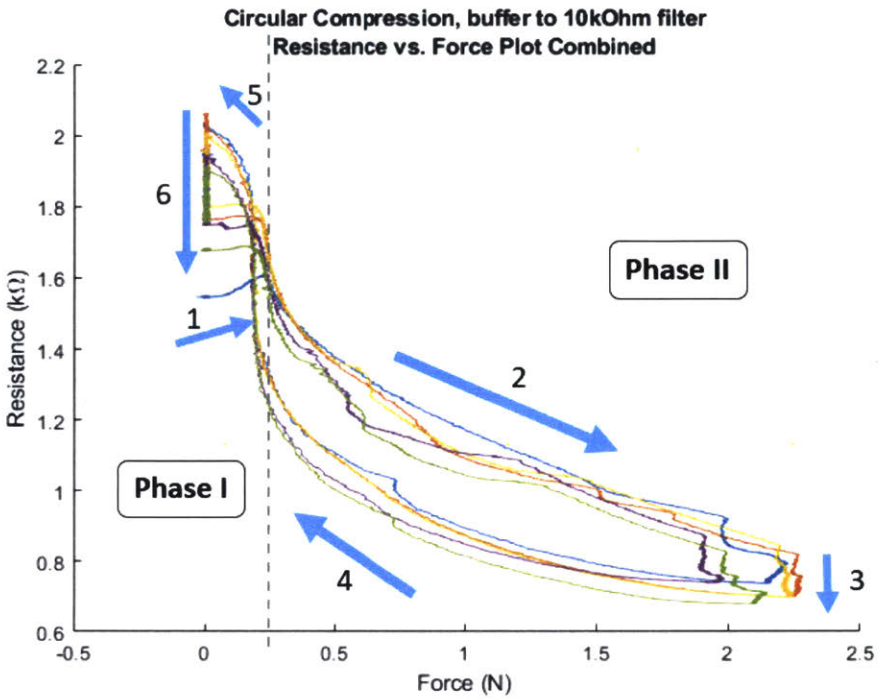

Figure 2-9: Point compression on spiral design. Each color represents a different trial on the same sensor. The sensor was compressed using the setup in Figure 2-8. At maximum extension, the tip is held at a constant load for 3s, and then the tip is slowly raised until it no longer contacts the sample. Finally, the sensor is monitored for 10s.

Zoflex CD45.1 Rubber

Since the carbon-black filled rubber had a two-phase resistance to force dependency, another type of rubber was investigated: Zoflex CD45.1 conductive rubber (Table A.2). A sheet of 1 mm thickness was used for the experiments in this section. The rubber is highly conductive with a volume resistivity of 0.1 Ω·cm., Shore A hardness of 45, and 50% elongation. When stretched beyond 30%, it plastically deforms and eventually tears.

A uniaxial tension test was conducted in an Instron, where the Zoflex rubber was cut into a dogbone shaped sample and clamped on both ends. Elongation and load was measured by the Instron. As the extension increased, the load also increased monotonically until a strain of 30% was achieved (Figure 2-10). After that, the load exerted by the sample would fluctuate up and down as the sample broke down and mechanical tears reduced the structural integrity of the material. The overall slope change also decreased, indicative of plastic deformation.

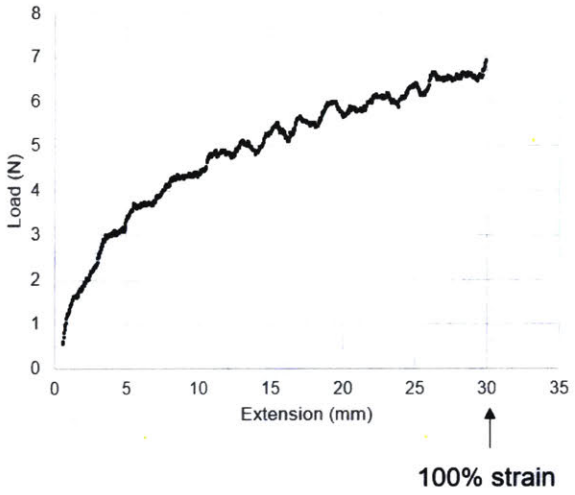

Figure 2-10: Uniaxial Tension for Mold Star 30 Rubber

While the material was being deformed, the effective resistance between the two ends of the dogbone were also monitored. Figure 2-11 shows the monotonic relationship between resistance and extension. Unlike the carbon-black rubber, the resistance always increases in response to strain. However, this relationship is not linear, with the resistance change being marginal with little extension, and an exponentially increasing resistance as the extension increases.

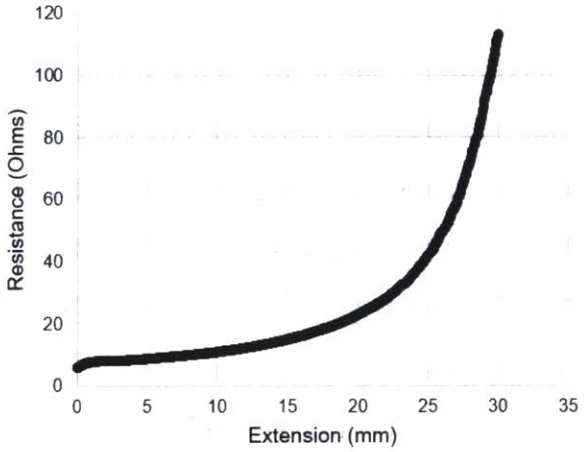

Figure 2-11: Uniaxial Tension for Zoflex CD45.1 Rubber

This rubber showed promise initially, but problems quickly arose. When the Zoflex rubber was molded in the Mold Star 30 rubber, it lost its conductive properties, and it became non-conductive, or the resistance increased to the MΩ regime. To remedy this,

a pocket in the mold was made to fit the shape of the Zoflex sensor, however, the sensor did not stick to the mold, resulting in unreliable readings. In addition, due to the microstructure of the material being composed of discrete balls, it is difficult to create clean, precise cuts using the vinyl cutter, since the material tends to tear in areas between the microbeads. This can be seen in the SEM image in Figure 2-1. The nonlinearities and low stretchability were two additional reasons why additional testing into this rubber was not pursued.

2.3 MathEarth Facility Testing

2.3.1 Pipe Network Configuration

In order to validate the 50mm and 100mm robots before conducting field tests, a facility was needed to provide a simulated environment to test these robots.

Requirements of the test facility:

- Flow and pressure regulation
- Insertion section must be able to insert the robot without causing damage
- Retrieval section must be able to remove the robot without causing damage
- Pipe section should be of constant diameter using Schedule 40 tubes and joints
- Pipe joints should not reduce the diameter of the water flow, so that the robot can pass through
- The pipe should have the following features
  - A valve to cut off the water supply
  - A spigot to simulate a leak of variable flow rate
  - A 3-foot removable section that can be swapped to simulate different environments, like a rusty pipe, a plastic pipe, or a leaky pipe

We submitted these recommendations to MathEarth, and over the period from October 2017 to February 2019, made the necessary upgrades. The following chapters highlight the tests we conducted during that time period, and the results and conclusions from the tests.

2.3.2 Testing Results

Upgrading the pipe network setup

The purpose of this test (April 6, 2018) was to upgrade the pipe structure to include pathways to test the 50mm and 100mm robots. This was the first time we took detailed measurements of the pipe configuration, including locations of the ball valves, the removable and permanent pipe joints, and dimensions of the pipes. The pipes were changed from a Chinese standard size to Schedule 40 pipes to be compatible with our robots. In addition, both the 50mm and 100mm sections had 3 foot removable pipe lengths that can be swapped to simulate different pipe conditions. A picture of the setup is shown in Figure 2-12.

To conduct a test of the 50 mm pipe, the valves to the 100 mm pipe are closed, the 50 mm robot is inserted in the lower left insertion point, and the robot is gently pushed into the pipeline. At this point the pump is turned on, initiating counter-clockwise flow through the system. This propels the robot forward, and it glides to the exit point. When the robot reaches the exit, the water is shut off, and the robot is retrieved using the robot retrieval mesh tool. This mesh is made of aluminum, and is curled into a cylinder and cut at a 45 degree angle, such that the robot is trapped but the water can flow through.

Trial Run with Upgraded Setup

In this demo on January 18, 2019, we went back to MathEarth to demonstrate that the 50mm robot can meet the design requirements. This included data sampling in a pipe network, as well as data analysis to show how the signals acquired correspond to the artificial leaks in the pipe. It was an opportunity for the MathEarth engineers to evaluate the robots through objective standards.

Figure 2-12: Experimental Pipe Network Setup at MathEarth's Acton Facility

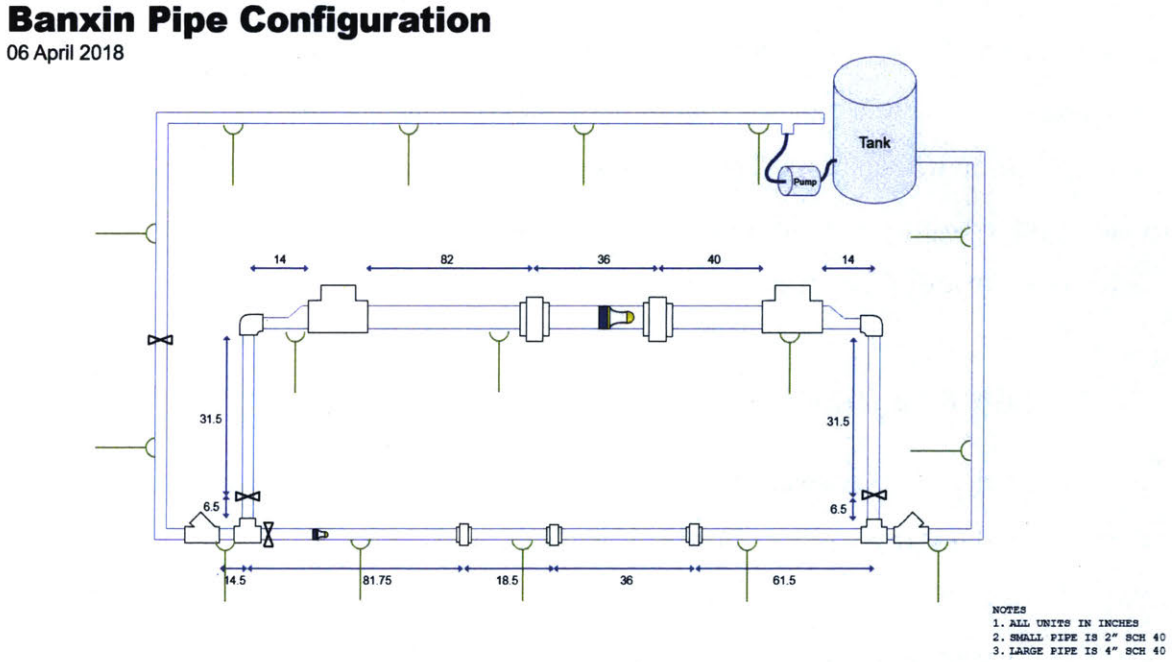

Figure 2-13: Pipe Configuration at MathEarth

We first tested the water pump to ensure that the 50mm test track itself worked properly. Then we did a trial run with the 50mm dummy robot, which ran without complica-

tion. Then we drilled a 1/4" hole in the middle of the pipe to simulate a leak, and ran the real robots for a couple trials while collecting data. After all the data was collected, we taught the MathEarth engineers how to offload the data from the robots, and used our Matlab script to interpret the data, identifying the start and end of the run, as well as a small peak that corresponded to the drilled leak site.

2.4 Leak Detection Test in Brazil

We partnered with Aegea Saneamento, a Brazilian sanitation company that manages all aspects of the water distribution cycle, from supply to collection to sewage treatment. Aegea was particularly interested in our robots' ability to detect small leaks in plastic pipes, since conventional methods are not capable of pinpointing leak locations. Our robot has the potential to localize itself within a pipe network, and feel along the pipe walls to discover leaks and report them before they turn into destructive and costly problems. Thus, Aegea invited the Mechatronics Research Lab to their headquarters in Matão, Brazil, four hours away from São Paulo, where we would have access to an operational residential pipeline that was constructed two years ago, but hadn't seen significant use in the two years. Thus it was a perfect opportunity to deploy our robots in a real-world network while minimizing disturbances to the community. Trip preparation details can be found in Appendix B.1.

2.4.1 Robot Fabrication

In order to meet the expectations of the Aegea group for testing, we had to learn how to fabricate and test these robots from scratch. The core technology was developed by You Wu, a former Ph. D. student in the lab [32], [34]. He produced a method for molding the body of the robots, fabricating the membrane sensors, and wiring the electronics.

To standardize the fabrication process between Elizabeth, Xiaotong, Steven, and myself, I created videos for the fabrication process, as well as the operational procedure, for internal use.

The construction of the robots follows a 15-step process, each detailed in 15 videos.

Figure 2-14: The Aegea-MIT Team, Matão, Brazil

1. Construction of the leak sensor
2. Fin assembly
3. Organize electronics on table
4. Connect SD card reader to microcontroller
5. Connect IMU to SD card reader
6. Connect the voltage regulator
7. Connect the analog-to-digital converter
8. Connect the wireless charging coil board
9. Connect the on/off button
10. Connect the wireless charging coil
11. Connect the four leak sensors
12. Connect the shunt resistors for the leak sensors
13. Connect the remaining electronics

14. Connect the battery and secure the electronics with hot glue

15. Pour silicone over the electronics in a mold, add clay to seal any leaks in the mold, and wait 24 hours

The 100mm robots follow the same procedure as the 50mm robots, but the mold used is larger, and the dimensions of the sensor are also scaled up. The 50mm robot in the mold is shown in Figure 2-15, and the 100mm robot outside of the mold is shown in Figure 2-16. After the robot is demolded, the neck area must be trimmed to make it more flexible. Then the robot is tested to be fully validated.

Figure 2-15: 50mm Robot in Mold

For a robot to be validated, it had to first demonstrate that it could be charged wirelessly. Next, it must demonstrate that it turns on. Next we had to check whether it connects to a computer directly for data offload, or whether it connects to a router that a computer can access. Finally we checked if it records comprehensible data and that the leak sensors and IMU work as expected.

Aegea also wanted us to validate the 50mm and 100mm pipes, so to have confidence that we could do multiple tests within both of these pipe diameters, it was critical to have a minimum of two functional robots of each size, and one dummy robot of each

Figure 2-16: 100mm Robot out of Mold

size. The dummy robot would be structurally identical to the function robot but it lacks electronics.

After these six robots were created and validated, the robots were charged and packaged into bubble wrap for transport.

In order to retrieve the robot at a T-junction, a wire mesh was curled into a cylinder, and one end was sliced at a 45° angle (Figure 2-17), such that the robot would hit the back end of the cylinder and be deflected up through the mesh, while water could pass through. This design was tested at MathEarth's facility. However, the wire mesh was ultimately not needed, since the water flow was completely diverted to spill out on land, such that the robot would not have to navigate any pipe junctions.

2.4.2 50mm Tests

The 50mm tests were conducted in the outskirts of town, situated on a hill (Figure 2-18). The distance between the inlet valve and the exit valve was 212m. These pipes were made of PVC plastic, and thus did not have any appreciable tuberculation. The pipe joints did not significantly change in diameter, so the robot would not be able to detect pipe joints. About halfway between the two valves is a house connection, which is a

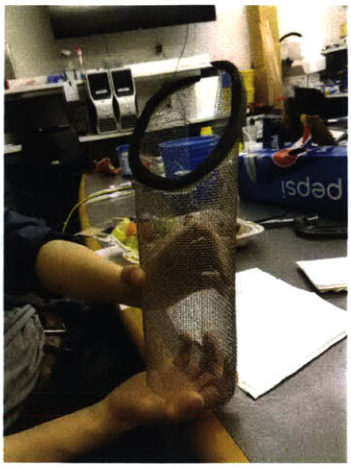

Figure 2-17: Wire mesh for robot retrieval

T-junction that a small pipe attaches to, from which homes can use the water (Figure 2-19.a). The flow rate from the house connection is much smaller than the bulk flow rate, but is on similar order to pipe leaks. An o-ring was installed improperly at the first vertical bend (Figure 2-19.b). Two slits were cut in the final horizontal pipe section to simulate cracks (Figure 2-19.c).

A section of the pipe just downstream of the first valve was split, so that the robot could be inserted into the pipe. A vertical bend was installed at the original pipe exit, and another right angle bend was installed to make the pipe horizontal again. An 18m length of pipe was attached to this horizontal section, and the robot would come out the other side.

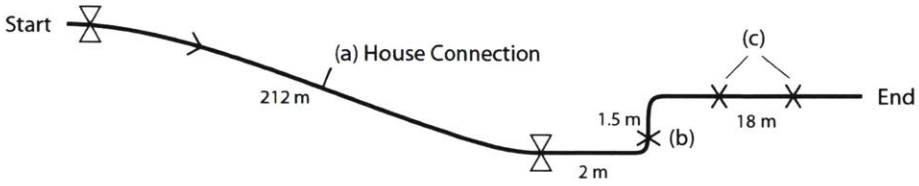

Figure 2-18: 50mm robot path with key features. (a) house connection, (b) improperly installed o-ring seal on vertical bend, (c) manmade linear cracks in pipe

The test procedure for all 50mm robots was as follows. The valve upstream was shut off, and the valve downstream was also shut off. A temporary sleeve was slipped over the cut region of the pipe, securing the pipe. The second valve was permanently opened fully so that the robot would pass through. The first valve was opened by unscrewing

the valve either one or two full revolutions. After the valves were opened, it took approximately 14 seconds for the water to start flowing out of the outlet. About 27 seconds before the robot exited, the rate of water flow coming out of the outlet increased significantly. Then the robot exited onto the grass, where we could retrieve it.

To fully inspect the pipeline, we first sent the 50mm dummy robot through to ensure that there are no obstacles that could damage the robot, and that the water pressure is sufficient to push it to the other end. Next, we sent both robots through the pipe. We noticed that when the water pressure was too great (upstream valve was opened two revolutions), the robot would not collect reliable data. Thus we throttled back the valve by only opening it one revolution in subsequent tests. We also opened the house connection in the middle of the pipe, in order to simulate an active use case where residents are tapping into the water supply during the inspection process. Thus two good trials were collected at the lower water pressure. The results are presented in section 2.4.5.

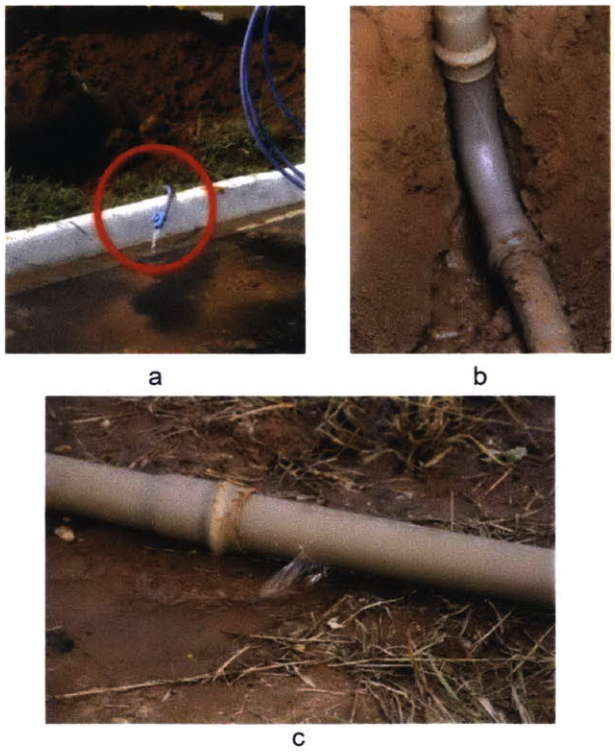

Figure 2-19: Leaks in 50mm pipe. a) house connection, b) improperly installed o-ring seal on vertical bend, c) linear cracks in pipe

2.4.3 100mm Tests

The 100mm tests were conducted on a flat residential street. The pipes were installed two years before we inspected them, but since homes were not built, there was not much use in this location. On the first day of testing, we soon realized that the water pressure in the pipe was much higher than the pressure we used in our test facility (greater than 2 bars above atmosphere). When we retrieved the robot, the data collection period was prematurely truncated. This led us to believe that the surge in water pressure when the main valve was opened caused the robot to shut off. Thus on the second day, we bypassed the button and forced the robot to always be in the data recording state. We tested the 100mm dummy robot once, and then sent the altered 100mm robot down the pipe twice. After trimming the data to correspond to the start and end times of the robots run, the shortened dataset was processed later using Matlab.

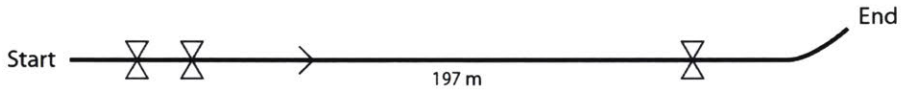

Figure 2-20: 100mm robot path

Figure 2-21: 100mm Robot Exiting Pipe

2.4.4 Data Analysis Methodology

The Matlab data analysis requrired a few key inputs:

1. Raw data from the robot (IMU, Leak Sensor Readings, Time)
2. Key features of the pipeline (such as length of pipe, estimated locations of key features like the position of the vertical segment in the 50mm section).
3. The voltage cutoff for identifying a leak, which is empirically determined by looking through the raw data

The start and end times that are manually recorded during the duration of the test were mapped onto the robot's recorded sensor readings. Key features in the pipe are correlated with the accelerometer data to further determine which part of the data corresponds to the different pipe sections. The code filters the leak sensor data to remove noise and drift, since the resistive-based sensors are sensitive to small vibrations. All sensors that record a pressure drop, and thus a resistance increase, are summed together. Resistance decreases were attributed to other pipe features, such as obstacles or pipe joints.

Next, multiple trials are correlated with windows of 0.25s, 1s, and 3s to identify the features that are most prominent across all the data sets. Therefore, a resistance increase that is consistent across multiple trials is indicative of a leak, whereas a resistance increase that only appears for one trial is less likely to be a leak.

For the purpose of data analysis, it did not matter which fin was pulled, since the robot is free to rotate as it traverses the pipe. In the future, the accelerometer data can be fused with the leak sensors to estimate which side of the pipe pulled on the sensor.

2.4.5 Results and Conclusions

50mm Tests

Two trials were collected from the second 50mm robot in the 50mm track. For data processing purposes, we divided the data into two periods: the section from the start

to the vertical section, and the vertical section to the end. After correlating the leak data between the two samples (Figure 2-22), three key features were identified in the first section. The first feature was located towards the beginning of the pipe, before the house connection. This may correspond to a leak. Next, about halfway through the track, another peak was identified. The location of this peak matched with the location of the house connection, showing that the robot was able to detect the presence of the house connection. However, it looked indistinguishable from a leak, so this means that the house connection locations should be known in order to properly interpret the data. This ambiguity is one of the focuses that the sensor described in Chapter 3 aims to address: by having a higher fidelity sensor to measure how the sensing sheet is deformed, it will be easier to differentiate leaks from house connections, obstacles, and other characteristics. Finally, there was another feature at the end of the data right before the vertical section. This overlaps with the location of the faulty house connection o-ring. However this spike may also be attributed to the pipe bend, since these features are coupled together in the present design. Again, the design in Chapter 3 will have even more information to decouple pipe bends and leaks. For now, we have shown that the leak sensing technology can identify key features in the pipe, and detect both known and unknown leaks.

For the second section, we cut two linear slits in the last section to act as artificial leaks. We knew the location of these leaks, so we could use it to validate the sensors and our localization method. There were two features identified in this section, one at 6.3m and one at 14.4m. This aligns with the measured locations of the two leaks: 6m and 12m (Figure 2-23). Thus we have confirmation that the sensors can respond to leaks and localize the leaks within a pipe system.

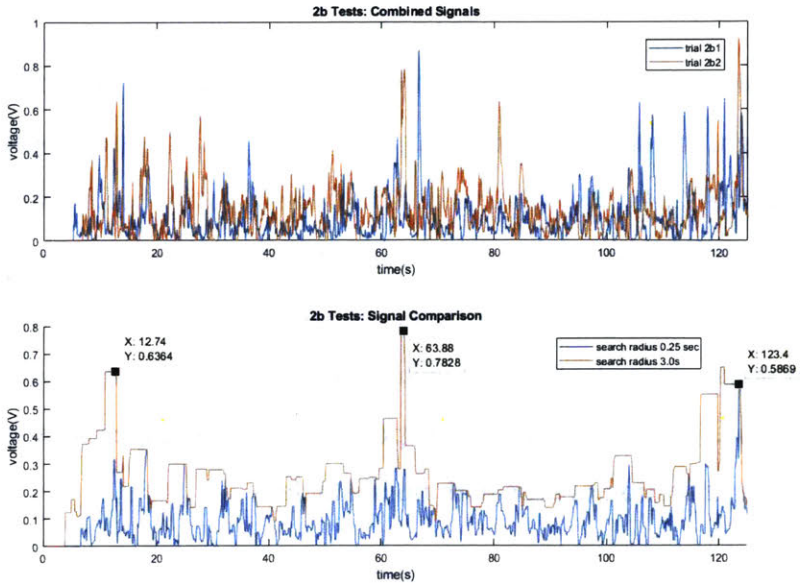

Figure 2-22: 50mm Data Signal Correlation for Main Pipe. (top) Sensor response for each run of the 50mm pipe, where each of the sensor readings were combined, and the time was linearly remapped to form a consistent time history of the run. (bottom) The similarity correlator algorithm that shows a peak if and only if signals from both runs has a peak in a given time frame, denoted as 'search radius' here.

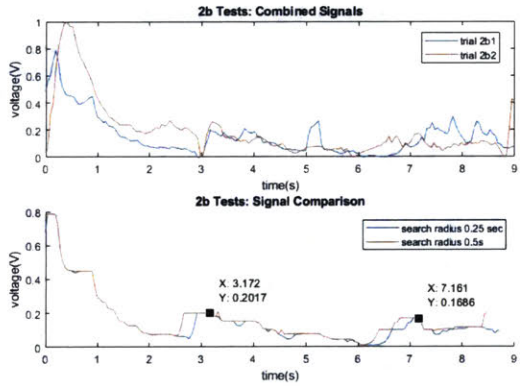

Figure 2-23: 50mm Data Signal Correlation for End Section. (top) Sensor response for each run of the 50mm pipe after the vertical section. In this section, there were two slits in the pipe that we added. (top) Each of the sensor readings were combined, and the time was linearly remapped to form a consistent time history of the run. (bottom) The similarity correlator algorithm shows peaks at 35% and 80% of the way through the pipe, while the actual leak locations were 33% and 66% of the way through the pipe. Note that there is a larger peak at the beginning of the dataset, and this is attributed to the robot experiencing high turbulence as the robot exits a pipe joint and the sensors must restabilize.

100mm Tests

For the 100mm pipes, there were no intentional leaks in the pipe network. After running the robots through, the signals from multiple trials were correlated together like in the 50mm tests (Figure 2-24). By running our matlab similarity correlator, there were no peaks that appeared for both trials at the same point in the pipe. Thus we concluded that no consistent abnormalities were detected, so the pipe was determined to not have any leaks. Any spikes in the leak sensor voltage was attributed to noise and not an actual feature of the pipe. This lack of leaks is expected, since the pipes were mostly unused, and it was a straight section of pipe with no obstacles.

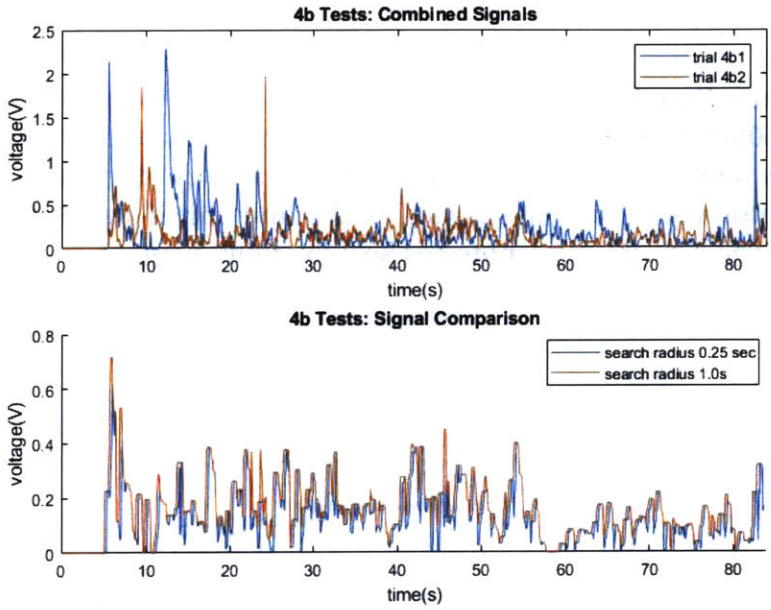

Figure 2-24: 100mm Data Signal Correlation. (top) Sensor response for each run of the 50mm pipe, where each of the sensor readings were combined, and the time was linearly remapped to form a consistent time history of the run. Note that the red and blue peaks do not overlap. (bottom) The similarity correlator algorithm detects no abnormality in the data, so it is concluded that there are no leaks.

2.5 Summary of Resistive Based Sensing

In this section, the piezoresistive sensors are characterized electrically and optically, various sensing geometries were explored, and a couple different fabrication methods were

tested. For these sensors, a mechanical load tester was used in conjuction with an Arduino based ohmmeter to determine the effective resistance of the sensor in different configurations, like in uniaxial tension and in radial tension. A Labview script was made to evaluate the sensor's performance in real time. Through these experiments, it was observed that the rubber operates in two regimes: the incompressible regime where the rubber increases resistance as it is stretched slightly, and the compressible regime where the rubber decreases resistance as it is stretched to a greater extent. Furthermore, different geometries trigger different regimes. Subjecting a vertical strip to a vertical pull test resulted in bypassing the first regime, so that increased force always decreased the resistance. However, pressing on the center of a planar spiral sensor caused both regimes to be prevalent. Thus, it is possible to produce geometries which have different force signatures. By overlapping sensors of different geometries in different orientations, it may be possible to calculate the direction and magnitude of an incident force.

To evaluate the usefulness of the resistance based sensing design, we went to Matão, Brazil to use the pipe networks Aegea provided for us. We first investigated a 50mm pipeline, and created three artificial leaks for the robot to detect. By running two trials and correlating the leak sensing data between the runs, the house connection, as well as all of the manmade leaks were detected. Furthermore, a leak was detected upstream of the house connection in both of the trials, indicating the presence of a leak or anomalous pipe feature. In the 100mm test, there were no strong peaks that both trials detected, so it was concluded that the pipe was in good condition with no major problems. Through the Brazil test, we have demonstrated that this robot can be useful in detecting and localizing leaks. However, we have also shown that it cannot differentiate a house connection from an improperly installed o-ring or a linear crack. Therefore, the sensor developed in Chapter 3 aims to provide a higher degree of freedom sensor that is able to decouple each of its bending modes, which can be used to characterize the objects the sensor is making contact with.

Chapter 3

Capacitive Sensor

The resistive based design in Chapter 2 demonstrated that it could be used to detect in-pipe features such as leaks and house connections. It has a suitable form-factor to brush up against the pipe wall, and respond to local pressure gradients. However, it also had some difficulty in characterizing the pipe features, relying on additional outside information to determine what feature each leak sensor reading corresponded to. Thus, it was important to develop other flexible sensing technologies that could also determine how the membrane is being stretched. After investigating many different technologies, the method I found to have the most potential was the capacitive sensor design.

The capacitive sensor has a couple key advantages over the resistive based sensors. For instance, the settling time constant is less than 0.1μs compared to over 10s for the resistive sensors. The response of the capacitive sensors are also linear, as opposed to the resistive sensors with a nonlinear response. The capacitive sensors also exhibit much less hysteresis and less overshoot. Furthermore, the capacitive sensors drift less over time than the resistive sensors.

Capacitive strain sensors were developed by other labs, like the Harvard Biodesign Lab [2]. However, their design is only able to determine how much it is being stretched as a linear scale, and cannot decouple different bending modes. There are other designs that can differentiate tension from bending, but cannot interpret twist or compression [19]. Thus there is a need to create a more versatile sensor that has sensing capabilities with more degrees of freedom.

Determining the unit sensor design parameters was an involved procedure involving many trials. A summary of these trials are listed in Appendix A in Table A.1.

3.1 Sensor Design

The goal of this membrane sensor was to be able to measure all the first-order bending modes of the sheet. Since the geometry of the sensor is a plate that is constrained along one edge, the sensor system exhibits four deformation modes: tension along the x-axis, compressive pressure along the z-axis, bending about the y-axis, and torsion about the x-axis (Figure 3-1). Since the sensor cannot provide a reaction force along the y-axis it will not show up in the result. Also curving about the z-axis is very difficult compared to the other bending modes, so it will not be measured as it has negligible contribution to the strain.

3.1.1 Sensor Geometry Optimization

It is important to ask what the minimum number of sensors is that can recover this information, and what arrangement of sensors would yield this property. For the following section, all unit sensors will be comprised of the capacitive fabric sensor as described in Section 3.1.2. Additionally, both the fabric and the silicone dielectric are much less elastic than the rubber substrate. Let's do a thought experiment to determine the sensor quantity and layout.

One Sensor

With one sensor, it is impossible to decouple bending and tension. The simplest configuration is a unit sensor that is constrained on the left edge. However, the unit sensor is only sensitive to tension, and bending the sensor causes no appreciable change in capacitance since neither the area nor the distance between the plates changes. Thus, this sensor can only detect tension. Furthermore, compression along z gives the same response as tension along x, and the sensor is not sensitive to torsion. Thus one sensor is not sufficient to detect the four modes.

Sensor #	Tension	Bending	Compression	Torsion
1	++	0	++	0

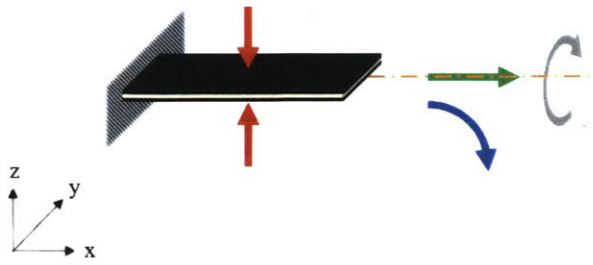

Figure 3-1: Fundamental Unit Sensor

Sensor #	Tension	Bending	Compression	Torsion
1	++	++	++	0

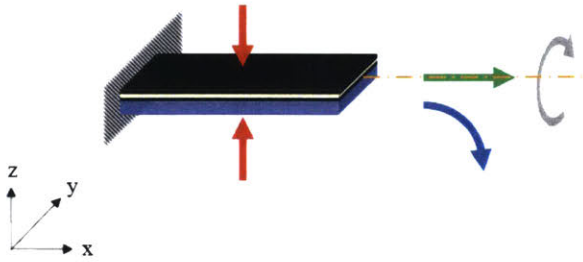

Figure 3-2: Unit Sensor on Substrate

With a single strip bonded to a stiffer, but still flexible substrate, tension in the x direction (green arrow) causes the capacitance to increase. Bending the sensor down, as indicated by the blue arrow, also causes the capacitance to increase. Bending the sensor up causes the capacitance to decrease. Thus, bending the sensor up while pulling will cancel itself out, producing no net change in capacitance.

Two Sensors

With two sensors, it is now possible to decouple bending and tension. However, it does not have enough information to determine if there is uniform compression on the sensor.

Let's look at the stacked sensor with two identical unit sensors on opposite faces

Sensor #	Tension	Bending	Compression	Torsion
1	++	++	++	0
2	++	−−	++	0

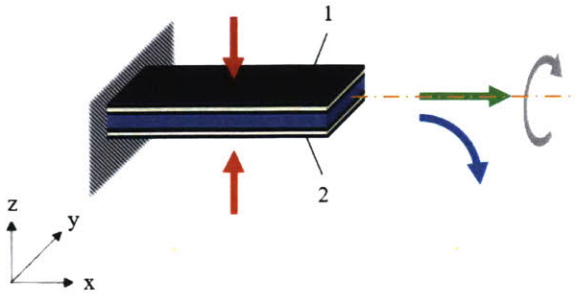

Figure 3-3: Two Sensor Stack

of the substrate as shown in Figure 3-3. In this configuration, uniaxial tension (green) causes sensor 1 and 2 to increase in capacitance. However, under bending (blue), sensor 1 increases and sensor 2 decreases. When bent the opposite way, sensor 1 decreases and sensor 2 increases. Thus, the average change in capacitance may be used to determine the tension, and the differential change in capacitance may be used to determine the bending. However, compression in the z-axis also affects the sensor in the same way as tension, by decreasing the space between the two plates. Thus, the sensor cannot differentiate uniaxial tension from compressive pressure. Furthermore, this sensor does not respond to torsion.

Now let's look at the two parallel sensor configuration as shown in Figure 3-4. This configuration has two sensors bonded to the same substrate. Uniaxial tension (green) causes sensors 1 and 2 to increase in capacitance strongly. Bending down (blue) causes sensors 1 and 2 to increase in capacitance similarly, while bending up causes sensors 1 and 2 to decrease in capacitance similarly. Uniform compression (red) causes sensors 1 and 2 to increase in capacitance similarly. However, torsion about the x-axis causes sensors sensors 1 and 2 to respond positively. This is in contrast to the stacked sensor configuration, which is not able to discern torsion. Unfortunately, all modes are coupled together, so it is impossible to differentiate which force was responsible for the response of the sensor.

Sensor #	Tension	Bending	Compression	Torsion
1	++	++	++	+
2	++	++	++	+

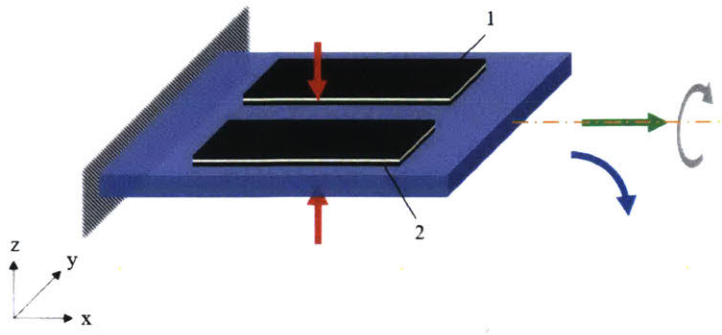

Figure 3-4: Two Sensors Side by Side

Three Sensors

Sensor #	Tension	Bending	Compression	Torsion
1	++	++	++	0
2	++	0	++	0
3	++	−−	++	0

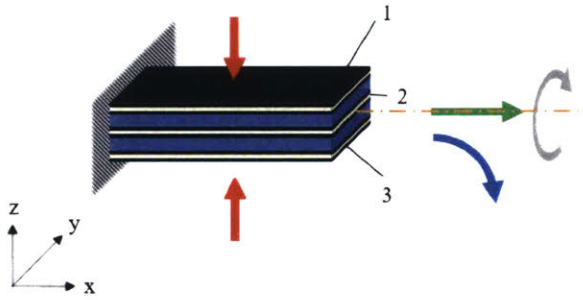

Figure 3-5: Three Stacked Sensors

With a third sensor, we can propose layouts that may provide more information regarding different bending modes. In this instance, let's investigate a three sensor layer design, since going from one layer to two layers increased the capabilities significantly. In uniaxial tension, sensors 1, 2, and 3 all increase at the same rate. In bending about the y-axis, sensor 1 increases capacitance, sensor 2 is neutral, and sensor 3 decreases capacitance. In uniform compression along the z-axis, sensors 1, 2, and 3 all increase at the

same rate. Additionally, torsion does not appreciably stretch the sensors, so there is no reaction. Thus sensor 2 is redundant and does not contribute any unique information.

Sensor #	Tension	Bending	Compression	Torsion
1	++	++	++	0
2	++	−−	++	0
3	+	+	++	0
(4)	+	−	++	0

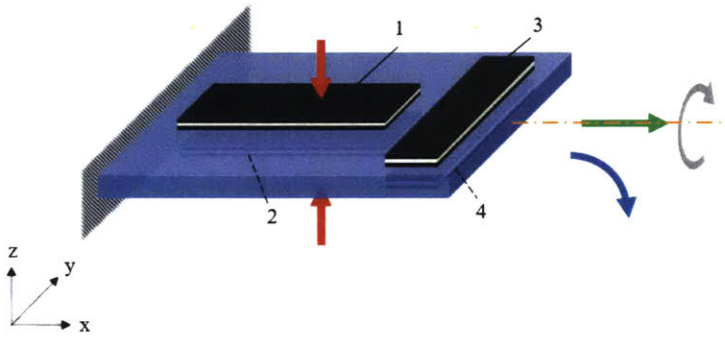

Figure 3-6: T Configuration

Rather than forming a triple stack, let's bond the sensor into a T configuration. In this layout, tension along the x-axis causes sensors 1 and 2 to respond strongly, while sensors 3 and 4 in the transverse direction respond weakly. Bending along the y-axis causes sensor 1 and 2 to curve the most, and will respond strongly with opposite signs. Sensors 3 and 4 will respond like sensors 1 and 2, but to a lesser degree since it is bending over a smaller arclength. Let's now consider the effect of uniform compression along the z axis: each sensor is subject to the same strain, so all sensors should behave uniformly. Finally, torsion does not appreciably affect the strain in the sensors, so torsion is not detectable in this configuration. Sensor 4 is redundant in this configuration, and is included here for symmetry. Thus, only sensors 1-3 are necessary to decouple tension, compression, and bending.

Four Sensors

The four sensor design (Sensors 1,2,3,5) in Figure 3-7 takes the best of all the previous sensors, and provides an arrangement that can differentiate tension, bending, torsion,

Sensor #	Tension	Bending	Compression	Torsion
1	++	++	++	+
2	++	−−	++	+
3	+	+	++	0
(4)	+	−	++	0
5	++	++	++	+
(6)	++	−−	++	+

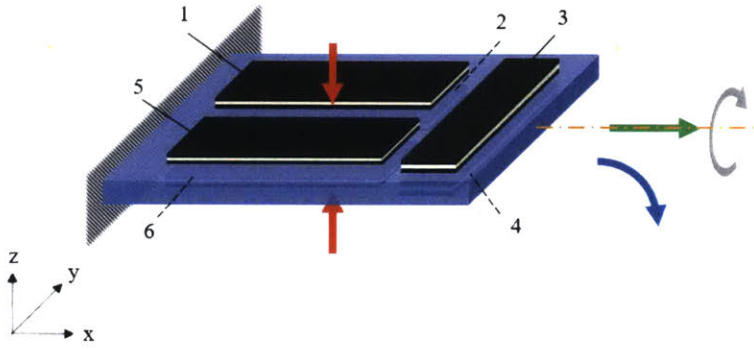

Figure 3-7: Omnidirectional Sensor

and compression. Two additional sensors (4 and 6) are incorporated for structural symmetry and added redundancy.

In uniaxial tension, sensors 1, 2, 5, and 6 are subject to the most deformation, so they will see the strongest response. Sensors 3 and 4 are oriented sideways, so they will still respond but to a lesser extent. In terms of bending (blue), the top sensors 1, 3, and 5 have a positive change, with sensors 1 and 5 responding the most. The bottom sensors 2, 4, and 6 have a negative change, with sensors 2 and 6 responding the most. When the bending direction is reversed, the sign of the changes is also reversed. For uniform compression, all six sensors are subject to the same strain, so they all show the same positive response. For torsion (gray), the sensors away from the axis of rotation show a positive change, namely sensors 1, 2, 5, and 6. The sensors that cross this axis, 3 and 4, show no response since they are not strained. Using all these sensitivity vectors from sensors 1, 2, 5, and 6, it is possible to recover which bending mode contributed to the capacitance changes.

Since this design proved to be sufficient for observing all four bending modes, these

sensors were incorporated into a larger sensor system in a dogbone shape (Figure 3-8). The dogbone shape was chosen so that the tensile test could be conducted. The following section details how the unit sensors and sensor system are fabricated.

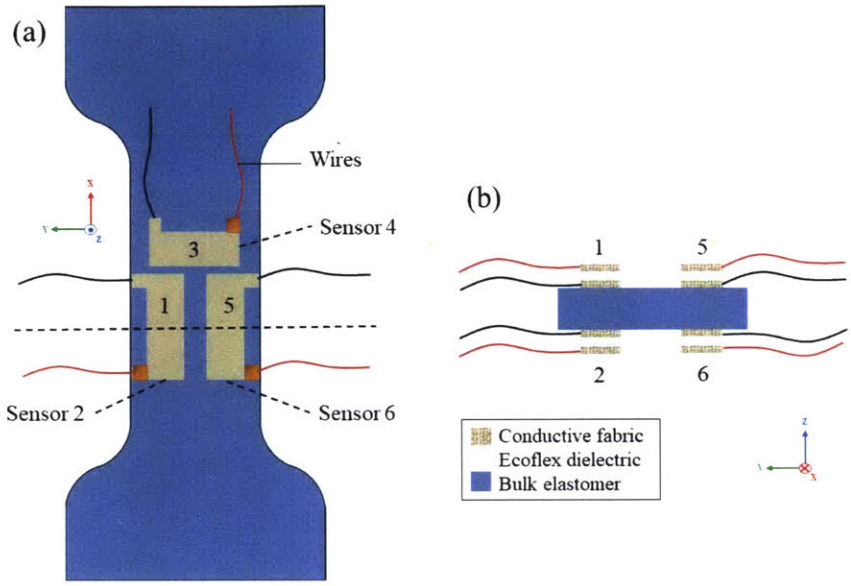

Figure 3-8: The layout of the dogbone sensor comprised of six individual sensors and wiring. (a) shows the top view of the sensor system, containing sensors 1, 3, and 5. (b) is the cross section view of the sensor system along the horizontal dashed line in (a). Sensors 2, 4, and 6 are mounted directly under sensors 1, 3, and 5, respectively.

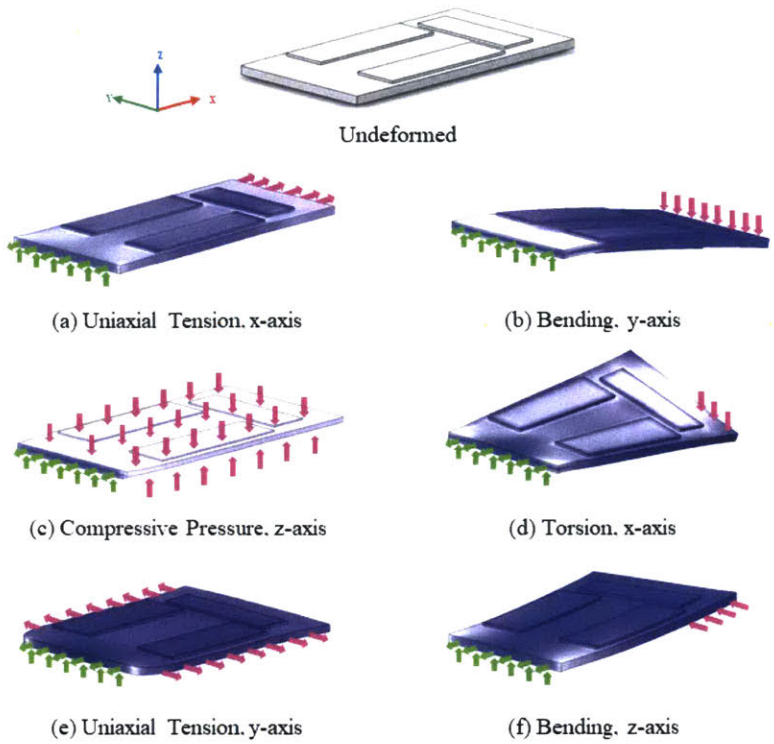

Figure 3-9: The strain distribution of the sensor system under (a) uniaxial tension along the x-axis, (b) bending about the y-axis, (c) compressive pressure on top and bottom surfaces along the z-axis, (d) torsion about the x-axis, (e) uniaxial tension on both faces parallel to the y-axis, and (f) bending around the z-axis. For all deformations (a)-(g), the same face is fixtured (green arrows). The color gradient from blue to white reflects the increasing magnitude of strain. Colors between images have different scales.

3.1.2 Unit Sensor Fabrication

This section describes the fabrication process for the unit sensor, and then presents the adhesion process to create the sensor system. Each capacitive sensor is comprised of two layers of highly conductive fabric that sandwich a silicone film that acts as the dielectric. In general, the film is created, and then the fabric is adhered to either side of the film, and the edges are cut with a laser cutter to ensure repeatability. The capacitance is affected by four factors, the electrode area (A), the thickness of the dielectric (d), the dielectric permittivity of vacuum (ϵ_0), and the silicone dielectric permittivity.

$$C_{sensor} = \varepsilon_0 k \frac{A}{d} \tag{3.1}$$

It can be shown that if the Poisson's ratio of the fabric is equal to the Poisson's ratio of the dielectric, which is the case if the two materials are mechanically bonded, then the capacitance with respect to uniaxial strain ε_x is as follows:

$$C_{sensor} = \varepsilon_0 k \frac{(1+\varepsilon_x) l_0 w_0}{d_0} \tag{3.2}$$

Since the textile also has an effect on the elastomer's bulk properties, each individual sensor may be more or less sensitive to uniaxial strain than predicted by this equation.

To create the film, Ecoflex 00-30 (Smooth-on, Inc.) is prepared according to package instructions, and is deposited into a 0.10 mm film on a metal surface using a thin film applicator. This layer is cured in an oven (Kenmore Elite 76771) at 65.6 °C for 20 min with air circulation (3-10a). Conductive silver plated nylon fabric knit in double direction (4900 Stretch Conductive Fabric, Holland Shielding, The Netherlands) is used as the electrodes. 1" wide copper tape with conductive adhesive (Kraftex, CA, USA) is attached to the fabric to form the tabs later (3-10b). An adhesive layer of 0.10 mm is applied on top the previously cured layer, and the prepared fabric is overlaid on top the adhesive layer. A metal roller is used to remove any air bubbles. This unit is cured in the oven at 65.6 °C for 20 min. The fabric and silicone is flipped over and air bubbles are removed. An adhesive layer of 0.10 mm is applied on top the silicone layer, and the prepared fabric is overlaid on top the adhesive layer, lining up with the fabric layer below. A metal roller is used to remove air bubbles. This unit is cured in the oven with the same heat treatment (3-10c).

To prepare the sensors for laser cutting, the fabric sensors are laid on a sheet of acrylic, and a piece of masking tape is applied to the top of the sensor. An Epilog laser cutter is used to cut the sensors with 30% speed, 50% power, and 50% frequency (Figure 3-10d). The laser cutter singes the edges of the sensor, mitigating the risk that the two fabric electrodes touch, which can happen when cutting the sensor with shears. In addition, the laser cutter provides more precise cuts which is not possible to achieve by

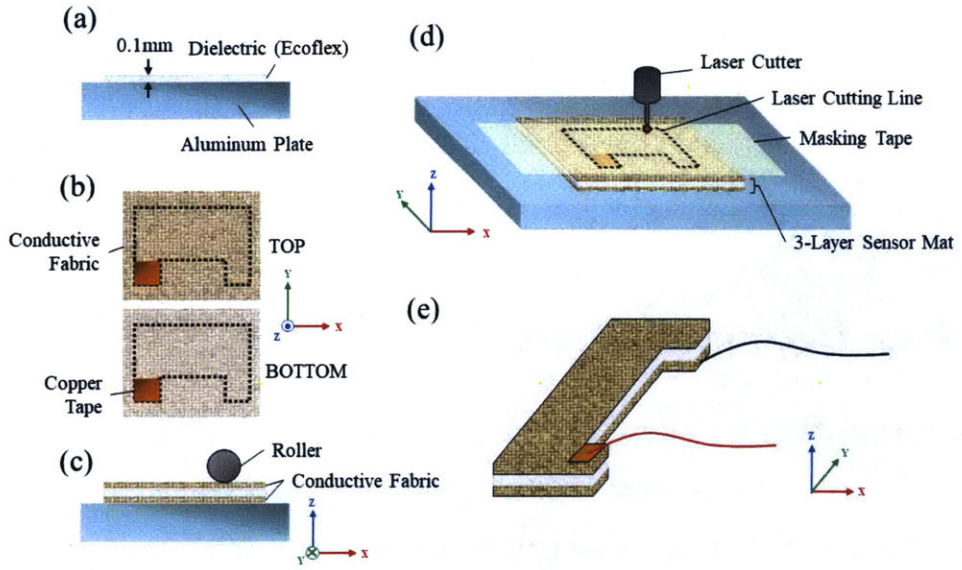

Figure 3-10: The fabrication procedure of a unit sensor. (a) 0.1mm-thick Ecoflex silicone layer is applied to the aluminum plate and is cured. (b) Conductive fabric is cut to Top and Bottom segments marginally larger than the size of the sensor. A 6mm x 6mm square copper tape is applied to both top and bottom fabric pieces. (c) The fabric pieces are placed on the top and bottom sides of the dielectric from (a). The copper tape on the Bottom fabric layer faces away from the dielectric. A roller is applied to ensure secure contact between layers. (d) Masking tape secures the 3-layer sensor mat from (c) onto the aluminum plate. Laser cutter then cuts along the sensor trajectory. (e) A complete sensor, with wires soldered to each of the two copper tape pieces. The same procedure is repeated for all 6 sensors.

hand. Next, tabs are cut which connect the sensor to the copper tabs. 30 AWG wires (Flexible Silicone Wire, Striveday) are soldered to the copper tabs (Figure 3-10e). The fabric layer on the opposite side of the tab is removed to remove the effect of the tabs on the sensor's capacitance.

3.1.3 Sensor System Fabrication

To create the sensor system, multiple of these sensors are arranged in a particular pattern. First, a 1.5mm thick layer of blue Mold Star 30 rubber (Smooth-On) in a dogbone shape is created using a 3D printed mold (Fortus 250 mc, Stratasys) from ABS, and cured in the oven at 65.6 °C for 30 mins. A 0.2 mm layer of Mold Star 30 rubber is spread on the

middle section of the dogbone, and three capacitive sensors are placed on top of this adhesive layer, with the wires going off to the side. For sensor 3 (as defined in Figure 3-8.a), the electrical tabs are supported by a metal scaffold so that it does not bond with the dogbone. This is cured in the oven at 65.6 °C for 20 minutes. The sensor system is flipped over, and sensors 2, 4, and 6 are laid out.

3.2 Four Decoupling Tests

The objective of the following experiments is to determine the relationship between relative capacitance change and each of the four bending modes (uniaxial tension, bending, pressure, and torsion) for each of the six sensors. Four experiments are conducted that sweep through various degrees of each deformation mode, and the resulting capacitance change is recorded and analyzed separately. All four sensitivity coefficients for each of the sensors are then used to define a method to decouple the four deformation modes.

3.2.1 Uniaxial Tension

The purpose of this test is to determine how each of the six unit sensors respond to uniaxial tension on the bulk substrate and determine each sensor's gauge factor, defined here as the change in capacitance per change in strain.

To create uniaxial tension, the dogbone sensor system was placed in a mechanical tester (Instron 5944, Instron, USA) with a 100 N load cell equipped with 250N pneumatic grips. The top of the dogbone was clamped between two 0.015" stainless steel plates to provide a uniform load, and the top grip was actuated. The load cell was balanced. The bottom of the dogbone was clamped between two 0.015" stainless steel plates, and the bottom grip was actuated. Slack was removed from the sample by raising the instron until zero load was achieved, at which point the gauge length was reset. A Sony RX100-M5 camera was set up on a tripod directly facing sensors 2, 4, and 6 so that strain across individual sensors could be measured. A capacitance-to-serial device (10-channel SPI Sensing Circuit, StretchSense, New Zealand) was used to capture capacitance values from

all six sensors simultaneously using the output data rate mode of 100 Hz with 0.1 pF resolution (Figure 3-11).

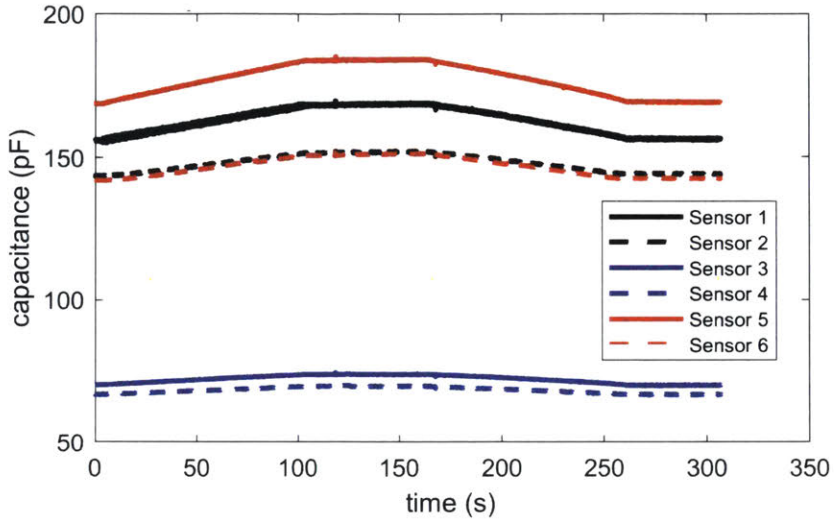

Figure 3-11: Capacitance vs. time for uniaxial tension test. The bulk elastomer is pulled with a strain rate of 9 mm/min, followed by a 30s hold, a relaxation rate of 9 mm/min, and another 30s hold. The curves show a linear relationship between uniaxial strain and the capacitance increase. Sensors 1, 3, and 5 have higher baseline capacitances and rates of increase than their counterparts 2, 4, and 6 which were mounted on the reverse side.

The crosshead was raised at a constant rate of 9 mm/min to a maximum extension of 15 mm. It was held there for 60 seconds, followed by a constant unloading rate of 9 mm/min to the original extension value.

The strains of each sensor was determined by analyzing the photographs. At maximum extension, sensors 1 and 2 experienced 4.87% axial strain and -2.55% transverse strain. Sensors 3 and 4 experienced 5.69% axial strain and -2.72% transverse strain. Sensors 5 and 6 experienced 4.71% axial strain and -2.98% transverse strain. The constant width section of the dogbone substrate experienced 6.98% axial strain and -4.19% transverse strain. The variation in the strains for the different regions means that the sensor pads have non-negligible effect on the strain. However, this is acceptable because each unit sensor is calibrated to its own sensitivity in this particular layout.

To determine the relationship between strain and capacitance, the signals from the capacitance sensing circuit and the Instron's strain and force readings were resampled

and mapped together. Due to rare, isolated errors in the serial bus that caused clear outliers in the capacitance reading, a Hampel filter with a 3 sample window was used to eliminate these outliers. A Savitzky-Golay filter of size 21 was used to smooth out the capacitance signal noise while doing delay alignment and mitigating transient effects at the start and end of the dataset.

We can also plot the relative change in capacitance against the input strain, defined as the gauge factor (Figure 3-12). For the range between 0-5% strain, the gauge factor is nearly identical between the extension and the relaxation profiles. Due to the viscoelastic properties of the silicone, there is a 5% creep in the steady-state capacitance, so the relaxation curve exhibits 0.005 more relative capacitance than the extension curve.

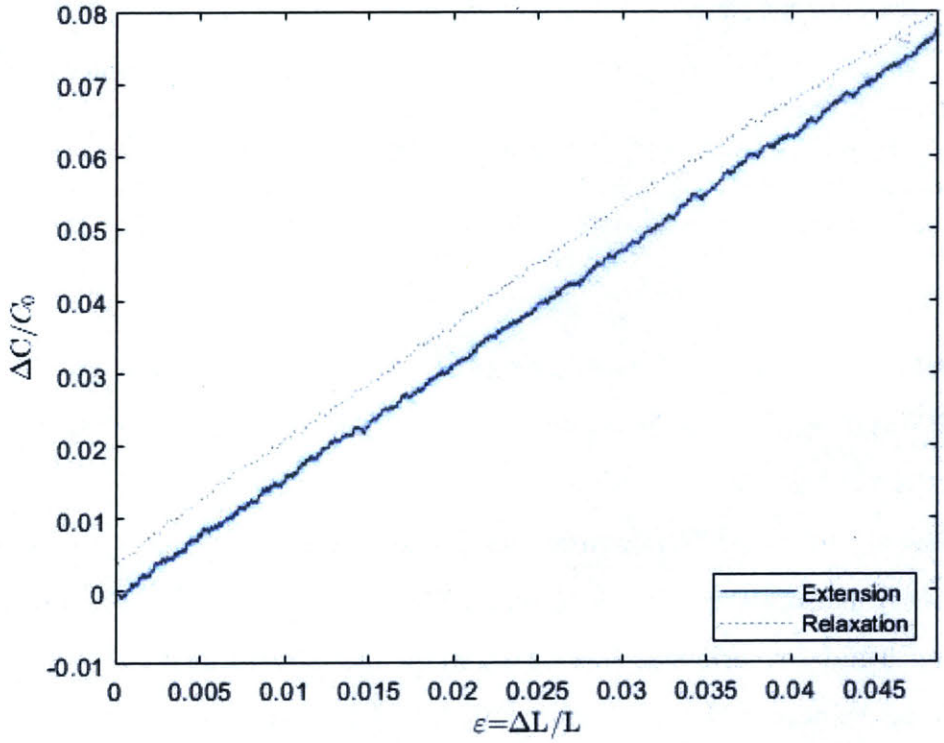

Figure 3-12: Relative capacitance change vs. strain for sensor 1. The capacitance change follows a linear profile with respect to the axial strain of sensor 1. It exhibits a 7.2% hysteresis width (which is approximately three times smaller than conductive silicone sensor system).

The gauge factors of each of the six sensors correspond to the calibrated sensitivities for each sensor with respect to uniaxial tension (Figure 3-13). Note that the gauge factor

for each sensor is greater than 1 for sensors 1, 2, 5, and 6, showing high sensitivity. Sensors 3 and 4 are oriented sideways, so they are not as sensitive to uniaxial tension along the tested axis by design. This trend is supported by the theory presented in the four sensor design on page 58, where sensors 1, 2, 5, and 6 respond more than sensors 3 and 4, while all the responses are positive.

It is also noteworthy that sensors 1, 3, and 5 are more sensitive than sensors 2, 4, and 6. This effect may be due to the even numbered sensor side having slightly more adhesive material, which increased the stiffness on that side. However, since the sensors are calibrated to themselves, it is not as important for the sensors to match exactly.

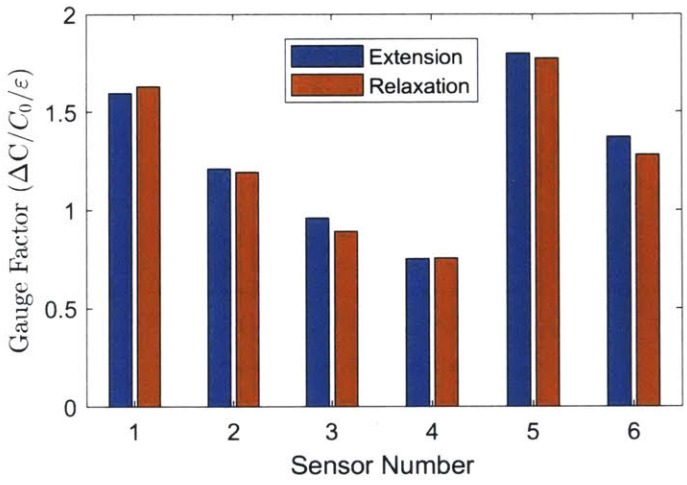

Figure 3-13: Summary of the change in relative capacitance per unit strain (gauge factor). The extension and relaxation curves are nearly identical, showing linearity of the system.

3.2.2 Bending

The purpose of this test is to determine how each of the six unit sensors respond to pure bending on the bulk substrate and determine each sensor's sensitivity factor, defined here as the change in capacitance per change in curvature.

To impart pure bending, the sensor system was laid on cylindrical PVC tubes of various radii. The long axis of the dogbone sample was wrapped around the tube. Masking tape was used to attach either end of the dogbone to the tube so that the sensor con-

formed to the cylinder geometry, without imparting tension along the long axis. The capacitance of the six sensors were measured simultaneously for at least 2 seconds using the output data rate mode of 100 Hz and 0.1 pF resolution. The capacitance was time-averaged, and the results for sensors 1 and 2, a representative sensor set, are shown in Figure 3-14.

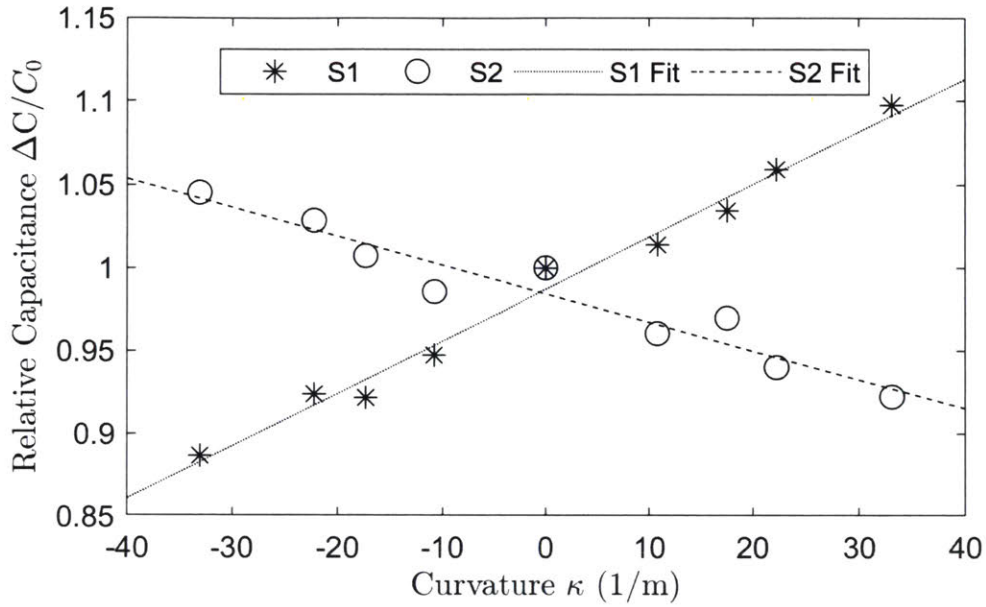

Figure 3-14: Relative capacitance change for various curvatures of sensor 1 (S1) and sensor 2 (S2), and the corresponding linear fits. Sensors 3-6 behaved similarly, and the sensitivity slopes are summarized in Figure 3-15.

From these graphs, it is evident that there is a linear relationship between the relative capacitance change and the curvature of the sensor. This is confirmed by the equation for the strain of a beam in pure bending:

$$\varepsilon = y * \kappa \tag{3.3}$$

where ε is the axial strain, y is the distance from the neutral axis, and κ is the curvature of the beam.

From the uniaxial tension test, we observe linearity between strain and capacitance change. Thus, the capacitance change is also proportional to the curvature. Furthermore, by having sensors above and below the neutral axis, the top sensors will have a

negative relative capacitance change relative to the bottom sensors. This confirms the theory explained in Section 3.1.1. The bend sensitivities are summarized in Figure 3-15.

As with the uniaxial tension test, sensors 2, 4, and 6 are less sensitive than sensors 1, 3, and 5. Also, sensors 3 and 4 are relatively less sensitive to bending than sensors 1, 2, 5, and 6 because of the rotated geometry of the sensor.

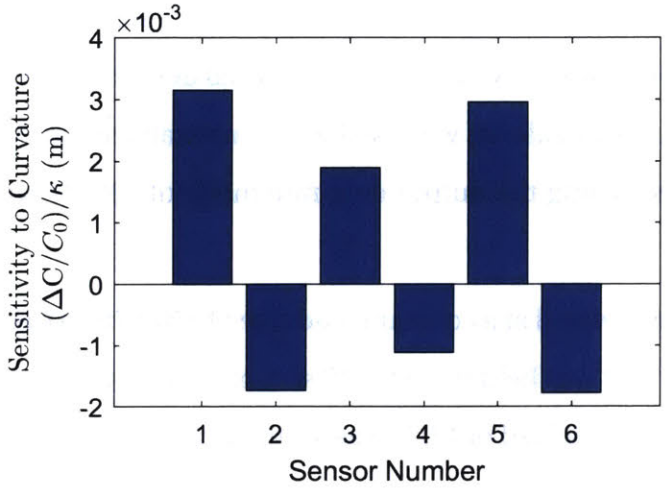

Figure 3-15: Summary of capacitance sensitivity per unit curvature for each sensor. Sensors 1, 3, and 5, which were mounted on the top of the bulk elastomer, show increased capacitance when subject to positive curvature since the top was under tension. Sensors 2, 4, and 6 were mounted on the bottom of the bulk elastomer, and they show decreased capacitance when subject to positive curvature since the bottom was under compression.

3.2.3 Compression

The purpose of the third test is to determine how each of the six unit sensors respond to planar compression along the z-axis, to simulate the bulk of the water pressure that the sensor would experience in a pipe. This test determines each sensor's sensitivity factor, defined here as the change in capacitance per change in load.

For the compression test, the dogbone structure is no longer needed, so the sides were sliced to turn the sensor into a rectangle that contain the six original strain sensors. This is henceforth referred to as the cropped sensor system. To produce a uniform compressive load on the cropped sensor system, the sensor is sandwiched between two acrylic sheets (69.07x43.41x3.18mm) that only cover the sensing region and leave the

tabs free to dangle off the side. The acrylic and sensor combination is placed on a 0.5" thick steel plate which is covered with paper to prevent electrical shorts. A mechanical tester (Instron 5944, Instron, USA) with a 2 kN load cell was used to press down on the sample. The crosshead was lowered until the compression plate made contact with the top layer of acrylic. The load cell was balanced and the gauge length was reset. A Sony RX100-M5 camera was set up on a tripod directly facing sensors 5 and 6 so that dimensions could be measured. A capacitance-to-serial device (10-channel SPI Sensing Circuit, StretchSense, New Zealand) was used to capture capacitance values from all six sensors simultaneously using the output data rate mode of 100 Hz with 0.1 pF resolution.

The crosshead was lowered at a constant load rate of 500 N/min to a maximum compressive load of 1500 N. It was held there for 30 seconds, followed by a constant unloading rate of 500 N/min until a load of 1.0 N was attained, and held for 30 seconds.

The signals from the capacitance tool and the Instron were mapped using the method in III.A, and the relative change in capacitance was plotted against the compressive load. For loads less than 150 N, the compressive load caused a linear increase in the relative capacitance (Figure 3-16), creating a linear gauge factor. This corresponds to a pressure of 50.0 kPa.

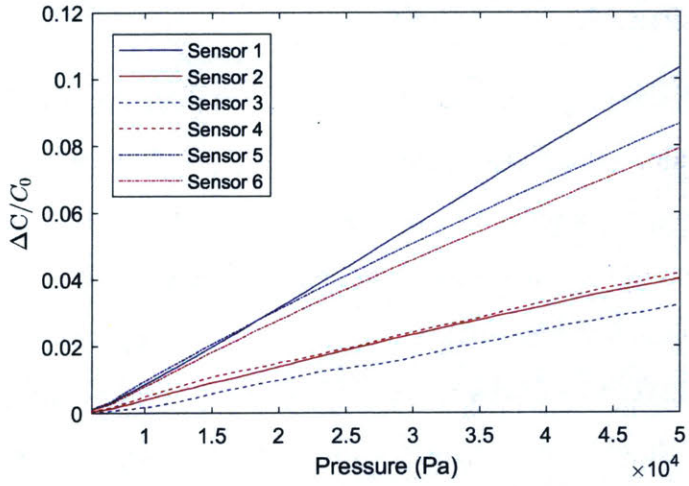

Figure 3-16: Relationship between relative capacitance change and compressive pressure. With pressures between 0 and 50 kPa, each of the six sensors are linear.

We can perform linear regression on this region to determine the relationship between relative capacitance change and pressure. The sensitivity results are displayed in Figure 3-17. From the theory in Section 3.1.1, all the sensors were expected to have similar responses. However, sensors 3 and 4 were less sensitive than the rest, possibly due to their unique geometry. While each of the sensors exhibit a positive capacitance change with increasing pressure, the rate of change is different than that of the uniaxial tension test.

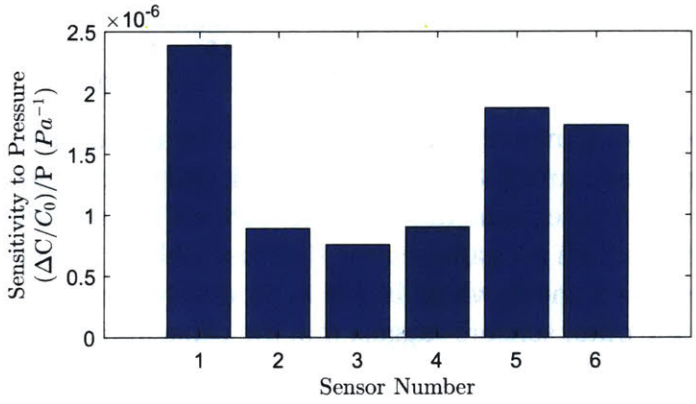

Figure 3-17: Summary of capacitance sensitivity per unit pressure for each sensor. Every sensor shows a positive linear relationship between pressure and capacitance. Sensors 1, 5, and 6, had particularly high sensitivity compared to sensors 2, 3, and 4, which may be due to small nonuniformities in the adhesive layer used to bond the sensor to the bulk elastomer. However, since the sensor still behaves linearly, this sensitivity vector is still used to normalize out the contribution of pressure to relative capacitance change.

We can subject the sensor to even larger compressions, ramping up to 1500 N, or 500 kPa. At this pressure scale, the sensor's capacitance change is no longer linear with respect to the compressive load (Figure 3-18). However, it is still a monotonic function, so a nonlinear one-to-one mapping may be produced from the capacitance to the applied pressure and vice versa.

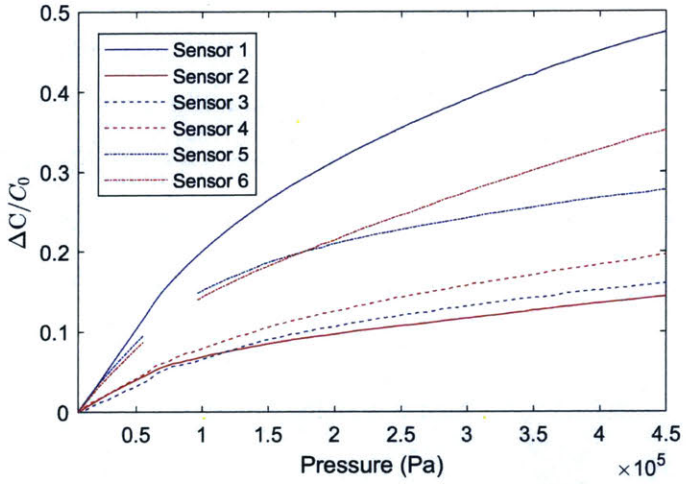

Figure 3-18: Relative capacitance change vs. pressure for all sensors. In this high-pressure test, loads between 0 and 450 kPa were induced, and the change in capacitance was subsequently recorded. The capacitance profile starts off linear until around 50 kPa, but then transitions into a high pressure regime that resembles a power law. There is a gap in the data for sensors 5 and 6, which is due to an unintended loss in data for this region, but data from the other sensors suggest that the capacitance increase should be smooth and continuous.

3.2.4 Torsion

The purpose of this test is to determine how each of the six unit sensors respond to pure torsion on the bulk substrate when clamped on two ends. We determine each sensor's sensitivity factor, defined in this section as the change in capacitance per change in torsional angle between the two clamps.

To create torsion, the cropped sensor system was placed in a mechanical tester (Instron 5944, Instron, USA) with a 100 N load cell. The sensor was clamped on one side by a rotating frame that spins when the Instron's crosshead is moved up and down. The other end of the sensor was clamped by a fixed mount, such that the sensor would rest horizontally when the Instron was set to the neutral point. The sensor was preloaded by distancing the fixed clamp apparatus from the rotating clamp. A capacitance-to-serial device (10-channel SPI Sensing Circuit, StretchSense, New Zealand) was used to capture capacitance values from all six sensors simultaneously using the output data rate mode of 100 Hz with 0.1 pF resolution.

The crosshead was lowered until the angle measurement measured -54.2° from hor-

izontal. The crosshead was raised at a constant rate of 140 mm/min to a maximum extension of 70 mm, corresponding to an angle of +48.9°. It was held there for 30 seconds, followed by a constant unloading rate of 140 mm/min to the original extension value.

Figure 3-20 shows the relationship between the twist angle and the relative change in capacitance for each sensor. Sensors 1 and 5 increased capacitance at a near linear rate when the sensor system was rotated to positive and negative angles. Sensors 5 and 6 increased capacitance linearly in positive angles, and decreased capacitance linearly in negative angles. Sensors 3 and 4 showed nearly no response to torsion. Since sensors 1 and 5 responded identically to both directions of twist, the sensor is capable of determining the absolute value of the torsional angle. Sensors 2 and 6 may be able to determine in which direction the sensor is being twisted. For the purpose of decoupling, the linearized equations will only account for absolute twist angle instead of signed twist angle. The torsional sensitivities are summarized in Figure 3-19.

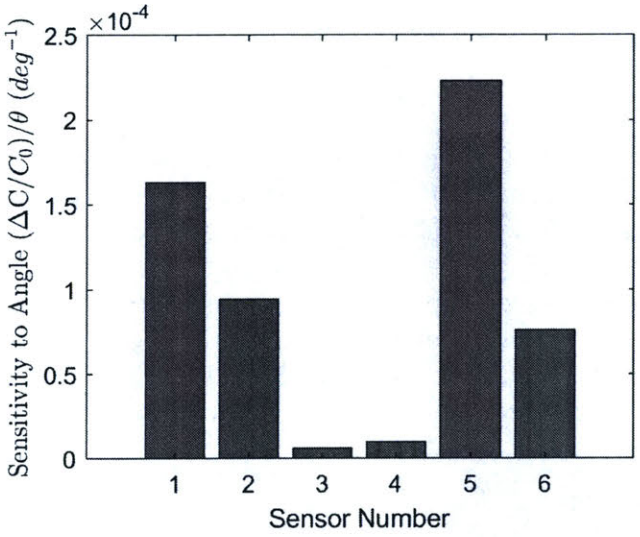

Figure 3-19: Summary of capacitance sensitivity with respect to absolute value of torsion angle. The sensors on the top (1, 3, 5) were more sensitive than the sensors on the bottom (2, 4, 6) because the bottom sensors had a thicker bonding layer of silicone between the blue substrate and the unit sensors.

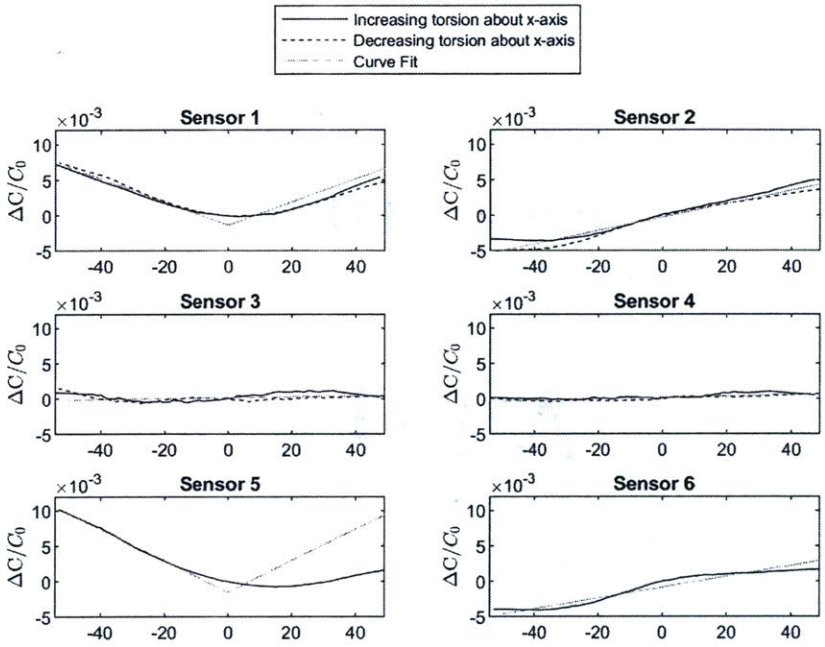

Figure 3-20: Relative capacitance change vs. torsion angle about the x-axis. All sensors behave nearly linearly with respect to the absolute value of the twist angle. Sensors 1 and 5, the top sensors on opposite sides of the x-axis show positive capacitance when twisted in either direction from neutral. Sensors 2 and 6, the bottom sensors on opposite sides of the x-axis, show a linear relationship between twist angle and capacitance. Sensors 3 and 4, the top and bottom sensors that cross the x-axis, show nearly no capacitive response to torsion. In sensor 5, it appears like the graph is symmetric about 15°instead of 0°, which may be due to residual stress in the system in the neutral orientation.

3.2.5 Decoupling Methodology

By noting the baseline values and contributions of each of the six sensors to each of the four deformation modes in isolation, for a general deformation we can identify how much of each bending mode contributed to the overall capacitance change. Since each of the deformation modes cause a linear change in capacitance for a given contribution from each mode (strain for tension, curvature for bending, pressure for compression, and angle for torsion), we can use linear algebra to decouple each of the four deformations given six sensor readings. Table 3.1 is a summary of the sensor contribution vectors

from sections 3.2.1-3.2.4.

Table 3.1: Sensor Response to Deformation Modes. The 6x4 array is equivalent to matrix S. Each column corresponds to the capacitance change contribution of each sensor to a particular deformation mode. These contribution coefficients were determined in sections 3.2.1-3.2.4.

Sensor No.	Deformation Mode ($\Delta C/C_0/x$)			
	Uniaxial Tension ($x = \varepsilon$)	Bending ($x = \kappa$)	Compression ($x = Pa$)	Torsion ($x = °$)
1	1.594	3.16×10^{-3}	2.392×10^{-6}	1.63×10^{-4}
2	1.209	-1.73×10^{-3}	0.891×10^{-6}	0.944×10^{-4}
3	0.960	1.90×10^{-3}	0.760×10^{-6}	0.064×10^{-4}
4	0.752	-1.11×10^{-3}	1.875×10^{-6}	0.101×10^{-4}
5	1.796	2.96×10^{-3}	1.732×10^{-6}	2.23×10^{-4}
6	1.372	-1.78×10^{-3}	1.900×10^{-6}	0.760×10^{-4}

Let the data be sensor response matrix, S, of dimensions 6x4, summarized in Table 3.1. Let d be the deformation contributed by each mode (tension, bending, compression, and torsion), expressed as a 4x1 matrix. Let c be the relative capacitance change from the baseline capacitance of each sensor, expressed as a 6x1 matrix. Assuming that c is a superposition of the individual deformations, which is valid because of the local linearity of each of the modes for small deformations, we can calculate c if we know S and d.

$$S \cdot d = c \tag{3.4}$$

To decouple the individual strains by knowing the relative capacitance change, we must solve for d. Since S is a non-square matrix, but we know that the columns of S are independent, we can calculate the pseudo-inverse:

$$S^{+} = (S^{T} \cdot S)^{-1} \cdot S^{T} \tag{3.5}$$

Thus,

$$d = S^{+} \cdot c = (S^{T} \cdot S)^{-1} \cdot S^{T} \cdot c \tag{3.6}$$

3.3 Summary

In this chapter, a fabric based capacitive sensor was designed with materials chosen to endure high maximum strains, elastic deformation, have a linear response, and be sensitive to tension and compression. Once the unit sensor was optimized, a layout composed of four critical sensors and two redundant sensors was created for the purpose of decoupling uniaxial tension, bending, torsion, and compressive pressure. Four separate experiments were conducted on the sensor, and the linear relationship between each deformation mode and sensor was determined. By assembling these sensor response coefficients into a matrix, the coupling and decoupling equations were established, providing a way to intuitively determine the types of forces acting on the sensor.

Chapter 4

Conclusion and Recommendations

4.1 Summary and Conclusions

In this thesis, two methods of designing a multi-axis tactile deformation sensor were investigated:

(1) a piezoresistive sensor with various geometries that excite different mechanoresistive behaviors of the sensor

(2) a capacitance based fabric sensor that can decouple uniaxial tension, bending, torsion, and compressive pressure

The resistive based method was evaluated in a real-world context by integrating them into a soft-bodied drone to investigate water pipes for leaks and other anomalous features. In the Matão, Brazil field test, it was determined that the sensing technology was able to identify leaks that were known, and point out other leaks that were not known at the time. Furthermore, it validated the leak detection robot system to be able to record data, survive the pipe conditions, transmit data, and localize the signals by mapping them onto the real pipe. This was an important test because it meant that the soft-bodied drone was a viable means of inspecting pipes. The test did reveal one key flaw in the resistive based approach: it could not, to high confidence, differentiate leaks, house connections pipe joints, obstacles, and faulty o-ring seals. This prompted an exploration into other tactile sensing technologies that could provide higher fidelity information about the bending mode of the sensor. Since the robot is able to traverse

long stretches of pipes while positioning a sheet sensor within 1 mm of the pipe wall, it made sense to focus attention onto improving the soft sensors.

After evaluating multiple sensor concepts, the capacitance based fabric sensor provided numerous advantages over other sensing methods, namely its linear response, fast sample rate, large deformation limit, and repeatability. These factors prompted an effort to use this technology to fabricate a generalized sensor system that could determine how a sheet was being stretched in any direction. By having this general sensor, it would be able to characterize the contact type of any object that touches it. After designing this sensor, it was tested in a universal testing system in four configurations: uniaxial tension, bending, torsion, and compressive pressure. It was shown that each of these deformation modes create a unique sensitivity vector that is linear with respect to the amount of bending. With linearly superposed deformations, a superposition of sensitivity vectors forms the resulting capacitance change. Likewise, we can determine the contribution from each bending mode from the resulting capacitance value using the method described in Section 3.2.5. This sensor system and decoupling methodology is the basis of the sensing method that has numerous applications.

This generalized deformation sensor can be used in leak detection because it is able to resolve differences between how it is being deformed. As discussed previously, leaks will cause positive uniaxial tension in the x-axis, and negative bending in the y-axis. Obstacles in the pipe cause positive bending in the y-axis, and possibly torsion along the x-axis if the obstacle does not contact the sensor uniformly. By positioning multiple of these sensor systems in a ring near the inner surface of a pipe, it is possible to scan the entire pipe simultaneously as the robot passes through. For example, the sensor system may replace the blue sensing fins on a flow driven drone like in [33], which is designed to measure the localized pressure gradient that a leak produces. This sensor has the advantages of being linear, having minimal hysteresis, being able to decouple all four shape deformations, not requiring sensor fusion with an IMU, and recording at over 250 Hz compared to 20 Hz. Furthermore, the bending angle from opposing pairs of sensor systems may be used to calculate the curvature of pipe joints as the robot passes through bends. As an extension, an additional sensor could be placed away from the

local pressure gradient to be used for calibrating the other sensors. Certain global properties like temperature will affect the dielectric constant of all the sensors, so having a sensor isolated from contact forces may be used for calibration.

4.2 Recommendations

In order to validate the sensor system for underwater leak detection, it must be waterproofed. This may be done by placing the sensor system in a mold and pouring Ecoflex 00-30 around the sensor system. Atalay et. al has shown this method creates a hermetic seal [2].

The sensor described in Chapter 3 can also be made more robust to environmental conditions. The copper tape method for affixing a wire to the sensor works for most conditions, but at large deformations the sensor may disconnect or become unstable. Thus, an alternative fabrication method is being investigated which involves sewing the wire to the fabric itself, and isolating the tabs from each other to avoid shorting the capacitor.

Once a robust, waterproof version of the sensor is fabricated, it may be implemented onto a robot or underwater test stand to characterize pipe features. In this realization, the deformation modes would show different responses depending on if the sensor passes over a leak, obstacle, or pipe joint. Through many trials, a dataset may be acquired to train a neural net to infer these features. Alternatively, it may be clear from the decoupled modes what type of feature the sensor has encountered. Either way, the additional information would make it possible to do a more detailed analysis of the interior of a pipe using only one trial and less a priori knowledge of the pipe layout.

Due to the general nature of this sensor, it may have many applications beyond leak detection. In particular, robot prehension is an area that could benefit from increased geometric modeling, as this sensor's decoupled measurements could be used to determine both the curvature of grasped objects, as well as the contact surface pressure. The torsion axis can provide additional information of the object's shape.

This sensor may be useful in wearable technology as well, particularly around human joints with multiple bending modes, like the wrist, shoulder, or hip. This would

enable high frequency measurements of the dynamic joint angle while minimizing the physical resistance for the user.

Appendix A

Tables

A.1 Capacitive Strain Sensor Fabrication Trials

Table A.1: Various iterations of the soft capacitive strain sensor. All sensors were made from Holland Shielding 4900 fabric, which has bidirectional stretch properties, and is highly conductive. Each turn is equivalent to a layer deposition height of 1/400 inches. 00-50 and 00-30 refer to products in the Ecoflex silicone line made by Smooth-On. Additionally, striveday wire was chosen because of its flexibility.

Name	Design	Dielectric	Additional Treatment
A	2 electrode, 1"x1" area, with copper tape tabs, magnet wire	00-50 8 turns base 5 turns adhesive	
B	2 electrode, 1"x1" area, with copper tape tabs, striveday wire	00-50 8 turns base 5 turns adhesive	Applied 00-50 coating to both sides for waterproofing Sprayed FlexSeal White Coated with yellow plastidip
C	2 electrode, 1"x1" area, with copper tape tabs, striveday wire, and coax wire	00-50 8 turns base 5 turns adhesive	
D	3 electrode, 1"x1" area, with copper tape tabs, striveday wire	00-50 8 turns base 5 turns adhesive	
E	2 electrode, 1"x0.27" area, with copper tape tabs, striveday wire	00-50 8 turns base 5 turns adhesive	Molded in vertical configuration
F	2 electrode, 1"x1" area, with copper tape tabs, striveday wire	00-50 8 turns base 5 turns adhesive	Blue Rubber
G	2 electrode, 1"x1" area, with copper tape tabs, striveday wire	00-50 8 turns base 5 turns adhesive	Liquid Electrical Tape
H	2 electrode, 1"x1" area, with copper tape tabs, striveday wire	00-50 8 turns base 5 turns adhesive	Plastidip direct
I	2 electrode, 1"x1" area, with copper tape tabs, striveday wire	00-50 8 turns base 5 turns adhesive	Tensile Test
J	2 electrode, 1"x1" area, with copper tape tabs, striveday wire	00-30 8 turns base 5 turns adhesive	
K	2 electrode, 1"x1" area, with copper tape tabs, striveday wire	Mold Star 00-30 4 turns base 5 turns adhesive	
L	2 electrode, 3"x3" area, with copper tape tabs, striveday wire	00-30 8 turns base 5 turns adhesive	
M	2 electrode, 1"x1" area, with copper tape tabs, striveday wire	00-30 4 turns base 5 turns adhesive	00-30 shell for non ASTM tensile test
N	2 electrode, 1"x1" area, with copper tape tabs, striveday wire	00-30 4 turns base 5 turns adhesive	for non ASTM tensile test
O	3 electrode, 1"x1" area, with copper tape tabs, striveday wire	00-30 4 turns base 5 turns adhesive	00-30 shell
P	3 electrode, 1"x1" area, with copper tape tabs, striveday wire	00-30 4 turns base 5 turns adhesive	00-30 shell
Q	2 electrode, 0.5"x1.5" area, lasercut, copper tape tabs, striveday wire (blue/yellow)	00-30 4 turns base 4 turns adhesive	
R	2 electrode, 0.5"x1.5" area, lasercut, copper tape tabs, striveday wire (red/green)	00-30 4 turns base 4 turns adhesive	

A.2 Materials List

Table A.2: List of materials used to make every sensor detailed in this thesis.

Vendor	Product	Description, Dimensions	Website
Stockwell Elastomerics	SE65-CON Rubber	Black carbon black filled conductive rubber, 1.0 mm thickness	https://www.stockwell.com/data-sheets/se65-con-conductive-silicone.pdf
Zoflex	CD45.1	Gray conductive rubber, 0.02" thickness, 12"x12"	http://www.zoflex.com/products.html
Stockwell Elastomerics	SNE556	65 Durometer Conductive Silicone Rubber with Nickel/Graphite Filler	https://www.stockwell.com/data-sheets/sne556-tech-data.pdf
Holland Shielding	4900 Stretch Conductive Fabric	Bi-directional conductive silver coated fabric, 300mm x 300mm	https://hollandshielding.com/Stretch-conductive-fabric
Tylson	Assurance Fabrics	Small 12" x 12" Highly Conductive Silver Fabric for Earth Connection/Grounding	https://www.amazon.com/gp/product/B01JR6SS1K/ref=ppx_yo_dt_b_asin_title_o07_s00?ie=UTF8&psc=1
Adafruit	Knit Jersey	Conductive fabric	https://www.adafruit.com/product/1364
Adafruit	Knit Conductive Fabric - Silver	Conductive fabric, 20cm x 20 cm	https://www.adafruit.com/product/1167
Smooth-On	Ecoflex 00-30	Most stretchable clear silicone, 10 psi (67 kPa) 100% modulus	https://www.smooth-on.com/products/ecoflex-00-30/
Smooth-On	Ecoflex 00-50	Very stretchable clear silicone, 12 psi (83 kPa) 100% modulus	https://www.smooth-on.com/products/ecoflex-00-50/
Smooth-On	Mold Star 30	Blue silicone, more rigid than Ecoflex, 96 psi (662 kPa) 100% modulus	https://www.smooth-on.com/products/mold-star-30/
Kraftex	Copper Tape	Copper foil tape with conductive adhesive, 1 in x 12 yd	https://www.amazon.com/Copper-Conductive-Adhesive-1inch-12yards/dp/B018RDZ3HG
Striveday	Wire	30 AWG	https://www.amazon.com/StrivedayTM-Flexible-Silicone-electronic-electrics/dp/B01KQ2JNLI/ref=sr_1_1_sspa?keywords=striveday+30+awg&qid=1557984728&s=gateway&sr=8-1-spons&psc=1
Gardner Bender	LTB-400	Liquid Electrical Tape	https://www.amazon.com/gp/product/B000FPAN2K/ref=ppx_yo_dt_b_asin_title_o04_s00?ie=UTF8&psc=1

Table A.3: List of fabrication tools used to make these sensors.

Vendor	Product	Description, Dimensions	Website
Silhouette	CAMEO 3	CNC Vinyl Cutter	https://www.silhouetteamerica.com/shop/machines/cameo
Silhouette	Autoblade	Cutting blade	https://www.silhouetteamerica.com/shop/blades-and-mats/SILH-BLADE-AUTO
Silhouette	CUT-MAT-12-3T	Cutting mat	https://www.silhouetteamerica.com/shop/blades-and-mats/CUT-MAT-12-3T
Stratasys	Fortus 250mc	FDM 3D Printer, prints ABSplus	https://support.stratasys.com/products/fdm-platforms/fortus-250mc
OMAX	2626	Abrasive Water Jet Cutting Machine	https://www.omax.com/omax-waterjet/2626
Epilog	Fusion 40	Laser Cutter	https://www.epiloglaser.com/laser-machines/fusion-laser-series.htm
Kenmore	Elite 76771	Digital countertop convection oven	https://www.amazon.com/gp/product/B075BDC39N/ref=ppx_yo_dt_b_asin_title_o09_s00?ie=UTF8&psc=1
NatSume Tech Store	SS Rolling Pin	Stainless steel rolling pin	https://www.amazon.com/gp/product/B07KG7JK36/ref=ppx_yo_dt_b_asin_title_o01_s00?ie=UTF8&psc=1
Gingher	8-in Dressmaker's Shears	Shears for cutting fabric	https://www.amazon.com/gp/product/B000UU6SR4/ref=ppx_yo_dt_b_asin_title_o03_s00?ie=UTF8&psc=1

Table A.4: List of test equipment used to evaluate these sensors.

Vendor	Product	Description, Dimensions	Website
Instron	5944	2 kN Capacity Universal Testing System	https://www.instron.us/en-us/products/testing-systems/universal-testing-systems/electromechanical/5900-series/5940-single-column
Instron	2712-052	250N Pneumatic Side Action Grips	https://www.instron.us/en-us/products/testing-accessories/grips/pneumatic-side-action-grips
Instron	2530-100N	100N Static Load Cell	https://www.instron.us/en-us/products/testing-accessories/load-cells/static/2530-series-static
Vernier	DFS-BTA	Dual-Range Force Sensor	https://www.vernier.com/products/sensors/force-sensors/dfs-bta/
Dremel	220-01 WorkStation	Rotary Tool Workstation Drill Press, for use in resistive sensor force gauge	https://www.dremel.com/en_US/products/-/show-product/tools/220-01-workstation
Gerneric	M4070 AutoRanging LCR Meter	LCR Meter up to 100H, 100mF, 20MR	https://www.amazon.com/Professional-M4070-ranging-Meter-Tester/dp/B018FRND0S
StretchSense	10-channel SPI Sensing Circuit	Capacitance to Serial converter for Arduino	https://www.stretchsense.com/stretch-sensors/

Appendix B

Event Documentation

B.1 Brazil Trip Preparation

B.1.1 Trip Logistics

In order to ensure a successful trip, we generated a packing list that would allow us to validate the robots we brought, and also gave us the ability to repair robots to any degree necessary. For instance, we planned to make minor repairs with sil-poxy rubber, and if needed, would have the capability to replace sensors and to re-mold the robots.

The packing list consisted of three categories: Essential technologies, repair tools and hardware, and materials for the robot retrieval tool.

Essentials: 2a, 2b, 2d (50mm Robots a, b and dummy d); 4a, 4b, 4d (100mm Robots a, b and dummy d); Wireless chargers x4, Power Supply, Laptop with working version of arduino and matlab, Laptop charger

Repair Kit: Wire stripper, Wire cutter, Multimeter, Pliers, Tweezers, Hot glue gun + hot glue, USB breakout board + microUSB chargers, Extra batteries (105mAh x2, 350 mAh x4), Extra sensors (2", 4"), Extra buttons, Extra chargers, SD Card + circuit board + adapter, IMU chip, Arduino/WeMos, Extra 3D printed parts (2" robot head, 4" robot head), Extra molding parts, Spare axles, Clay, Wire (flexible + solid core), Heat shrink tubing, Krazy glue, Sil-poxy, 00-50 Rubber

Robot Retrieval Tool: Wire Mesh Clipper, Fishing Line, Wire mesh, Needle, Grasper

Tool, Rubber

Soldering iron and solder were provided by Aegea.

B.1.2 Tour of Aegea Headquarters

Elizabeth and I arrived at the Sao Paulo International Airport on August 6, 2018 at 9 AM. Vinicius Jacques da Silva, a manager at Aegea, was our primary point of contact for the trip. He brought us to the company's administrative center in Santa Bárbara d'Oeste. At this facility, we met with some of the regional managers who gave a presentation about the state of the water management technologies, real-time monitoring software, and a visual representation of how much water was being lost per region. Some of these regions experienced losses of 40%, making these zones high priority to fix. However, finding the leaks are a non-trivial problem, so a technology such as ours would be extremely useful and cost-effective to Aegea.

B.2 HUBweek Boston

On October 12, 2017, We represented MIT's MechE department at HUBweek in Boston. This was an opportunity to present our work to the public, and cater our demo to a diverse audience of different technical backgrounds and demographics. In addition, it was a chance to use non-technical language to convey both the magnitude of the issue of pipe leak detection as well as our lab's solution to the problem. We also brought a live demo, where the robot could communicate with a computer in real-time, broadcasting its leak sensor values. The live demo also allowed people to visually see how the robot was able to bend around corners, and visitors could feel the silicone body to imagine how it can deform around in-pipe obstacles.

Figure B-1: Hubweek Boston's MIT demo booth with me, Elizabeth Mittmann, and You Wu.

Appendix C

Code

C.1 Data Processing for Uniaxial Tension

All code in this section was executed in MATLAB R2017b. This code documents how to interpret the raw capacitance, strain, and load values, and determine how sensitive each sensor is to uniaxial tension. The code also plots the graphs. The code for the other three bending modes are very similar to this code, with slightly different graph outputs.

```
% Reading Capacitance Log Files From Tension Testing

% Savitzky-Golay Filtering info at
% https://www.mathworks.com/help/signal/examples/signal-smoothing.
% html?prodcode=SG&language=en

clear variables;
close all;

% Import Data from Capacitance to Digital reader

basicpath = 'C:\Users\musub\Dropbox (MIT)\MIT\Mechatronics ...
    Lab\UROP - Jiyoung\Capacitance Log Files\Cleaned Data\';
%adjust the basicpath based on what computer you're using
filename = '0222-165308-Cap';
```

```
15 extension = '.log';
16 file1 = [basicpath, filename, extension];   %connect path and file
17
18 data = importdata(file1,',',2);
19 dataCH1 = data.data(:,1);
20 dataCH2 = data.data(:,2);
21 dataCH3 = data.data(:,3);
22 dataCH4 = data.data(:,8);
23 dataCH5 = data.data(:,5);
24 dataCH6 = data.data(:,9);
25
26 % Time remapping keyframes from Arduino Cap-to-Digital
27 t_1 = 1087;      % start of extension ramp
28 t_2 = 29590;     % end of extension ramp
29 t_3 = 47060;     % start of relaxation ramp
30 t_4 = 74760;     % end of relaxation ramp
31 t_5 = 88362;     % end of data
32
33 t_a = 1;
34 t_b = 2002;
35 t_c = 3205;
36 t_d = 5205;
37 t_e = 5806;
38
39 % Import Data from Instron
40
41 basicpath_instron = 'C:\Users\musub\Dropbox ...
       (MIT)\MIT\Mechatronics Lab\UROP - Jiyoung\Instron Raw ...
       Data\02-22 Uniaxial Tension\0222-1535.is_tcyclic_RawData\';
42 filename_instron = 'Specimen_RawData_5';
43 extension_instron = '.csv';
44 file2 = [basicpath_instron, filename_instron, extension_instron];
45
46 data_instron = xlsread(file2);
47 data_instron_time = data_instron(:,1);
48 data_instron_ext = data_instron(:,2);
```

```
data_instron_load = data_instron(:,3);

% Defaults for this document
width = 5;      % Width in inches
height = 3;     % Height in inches
alw = 0.75;     % AxesLineWidth
fsz = 11;       % Fontsize
lw = 0.5;       % LineWidth
msz = 8;        % MarkerSize

%then do the below code
%% Processed Data

% Extension to Strain
% CH2: 4.71% for 15mm
strain_factor2 = .0487/15;
strain_factor4 = .0569/15;
strain_factor6 = .0471/15;

figure(1)
pos = get(gcf, 'Position');
set(gcf, 'Position', [500 200 5*100, 3*100]); %<- Set size
set(gca, 'FontSize', fsz, 'LineWidth', alw); %<- Set properties
[strain1a,cap1a,strain1b,cap1b] = capVsStrain(dataCH1(t_1:t_2), ...
    dataCH1(t_3:t_4), data_instron_ext, t_a, t_b, t_c, t_d, ...
    strain_factor2);
graphCapVsStrain(strain1a,cap1a,strain1b,cap1b,filename,'1')
p1a = polyfit(strain1a(601:1400),cap1a(601:1400),1)
p1b = polyfit(strain1b(601:1400),cap1b(601:1400),1)

print('tension-sensor1','-dpng','-r300');

figure(2)
[strain2a,cap2a,strain2b,cap2b] = capVsStrain(dataCH2(t_1:t_2), ...
    dataCH2(t_3:t_4), data_instron_ext, ...
    t_a,t_b,t_c,t_d,strain_factor2);
```

```
graphCapVsStrain(strain2a,cap2a,strain2b,cap2b,filename,'2')
p2a = polyfit(strain2a(601:1400),cap2a(601:1400),1)
p2b = polyfit(strain2b(601:1400),cap2b(601:1400),1)

figure(3)
[strain3a,cap3a,strain3b,cap3b] = capVsStrain(dataCH3(t_1:t_2), ...
    dataCH3(t_3:t_4), data_instron_ext, ...
    t_a,t_b,t_c,t_d,strain_factor4);
graphCapVsStrain(strain3a,cap3a,strain3b,cap3b,filename,'3')
p3a = polyfit(strain3a(601:1400),cap3a(601:1400),1)
p3b = polyfit(strain3b(601:1400),cap3b(601:1400),1)

figure(4)
[strain4a,cap4a,strain4b,cap4b] = capVsStrain(dataCH4(t_1:t_2), ...
    dataCH4(t_3:t_4), data_instron_ext, ...
    t_a,t_b,t_c,t_d,strain_factor4);
graphCapVsStrain(strain4a,cap4a,strain4b,cap4b,filename,'4')
p4a = polyfit(strain4a(601:1400),cap4a(601:1400),1)
p4b = polyfit(strain4b(601:1400),cap4b(601:1400),1)

figure(5)
[strain5a,cap5a,strain5b,cap5b] = capVsStrain(dataCH5(t_1:t_2), ...
    dataCH5(t_3:t_4), data_instron_ext, ...
    t_a,t_b,t_c,t_d,strain_factor6);
graphCapVsStrain(strain5a,cap5a,strain5b,cap5b,filename,'5')
p5a = polyfit(strain5a(601:1400),cap5a(601:1400),1)
p5b = polyfit(strain5b(601:1400),cap5b(601:1400),1)

figure(6)
[strain6a,cap6a,strain6b,cap6b] = capVsStrain(dataCH6(t_1:t_2), ...
    dataCH6(t_3:t_4), data_instron_ext, ...
    t_a,t_b,t_c,t_d,strain_factor6);
graphCapVsStrain(strain6a,cap6a,strain6b,cap6b,filename,'6')
p6a = polyfit(strain6a(201:1000),cap6a(201:1000),1)
p6b = polyfit(strain6b(201:1000),cap6b(201:1000),1)

```

```
curvefits = [p1a p1b;
             p2a p2b;
             p3a p3b;
             p4a p4b;
             p5a p5b;
             p6a p6b]

figure(7)
bar([curvefits(:,1),curvefits(:,3)])
ylabel('Gauge Factor ...
    ($\Delta$C/$C_0$/$\varepsilon$)','Interpreter','latex')
xlabel('Sensor Number')
title('Sensitivity to Uniaxial Tension by Sensor')
legend('Extension','Relaxation','location','North')

%% Raw Data
figure(100)
pos = get(gcf, 'Position');
set(gcf, 'Position', [500 200 5*100, 3*100]); %<- Set size
set(gca, 'FontSize', 8, 'LineWidth', 3); %<- Set properties
time = linspace(0,306.8125,88362);
plot(time,hampel(dataCH1),'k-','LineWidth',2);
hold on
plot(time,hampel(dataCH2),'k--','LineWidth',2);
plot(time,hampel(dataCH3),'b-','LineWidth',2);
plot(time,hampel(dataCH4),'b--','LineWidth',2);
plot(time,hampel(dataCH5),'r-','LineWidth',2);
plot(time,hampel(dataCH6,5),'r--','LineWidth',2);
%plot(data.data(:,7),'-');
xlabel('time (s)');
ylabel('capacitance (pF)');
title('Capacitance vs. Time for Uniaxial Tension Test');
aa = legend('Sensor 1', 'Sensor 2', 'Sensor 3', 'Sensor 4', ...
    'Sensor 5', 'Sensor 6', 'location', 'East')
aa.FontSize = 8;
ylim([50 200])
```

```
143 savefig([basicpath, filename,'-graph.fig'])
144
145 print('tension-allSensors','-dpng','-r300');
```

This subroutine performs time remapping on the raw data, normalizes the extension value to become strain, and normalizes the capacitance value to be relative capacitance change.

```
1 function [strainA,capA,strainB,capB] = capVsStrain(cap12, cap34, ...
      extension, t_a,t_b,t_c,t_d,strain_factor)
2     [t12,y12] = time_remap(cap12,t_a,t_b);
3     strainA = (extension(t_a:t_b-1)-extension(t_a))*strain_factor;
4     capA = y12'/y12(1)-1;
5     [t34,y34] = time_remap(cap34,t_c,t_d);
6     strainB = (extension(t_c:t_d-1)-extension(t_a))*strain_factor;
7     capB = y34'/y12(1)-1;
```

This subroutine performs the time remapping. Given a set of data, it will create a time sequence that linearly remaps it to the desired start and end times. This is useful to correlate the instron data with the capacitance data, which are recorded separately and must be aligned.

```
1 function [t2,y3] = time_remap_matrix(y,ta,tb)
2     y = hampel(y);
3     fs = length(y)+20
4     fsResamp = tb-ta+20;
5
6     ypad = [repmat(y(1,:), 10, 1); y; repmat(y(end,:), 10, 1)];
7
8     vResamp = resample(ypad, fsResamp, fs);
9     tResamp = (0:size(vResamp,1)-1) / fsResamp;
10    %y3 = vResamp(11:end-10);
11    y3 = sgolayfilt(vResamp(11:end-10,:),1,11); % after filtering
12    t2 = linspace(ta,tb-1,fsResamp);
```

This subroutine graphs the strain vs. relative capacitance change for one sensor.

```
function [] = graphCapVsStrain(strain1a, cap1a, strain1b, cap1b, ...
    filename, SensorNo)
    plot(strain1a,cap1a,'-')
    hold on
    plot(strain1b,cap1b,':')
    ylabel('$\Delta$C/$C_0$','Interpreter','latex')
    xlabel('$\varepsilon$=$\Delta$L/L','Interpreter','latex')
    legend('Extension','Relaxation','Location','SouthEast')
    xlim([0 inf])
    title(['Relative Capacitance Change vs. Strain, Sensor ', ...
        SensorNo])
```

Bibliography

[1] Morteza Amjadi, Ki-Uk Kyung, Inkyu Park, and Metin Sitti. Stretchable, Skin-Mountable, and Wearable Strain Sensors and Their Potential Applications: A Review. *Advanced Functional Materials*, 26(11):1678–1698, 3 2016.

[2] Asli Atalay, Vanessa Sanchez, Ozgur Atalay, Daniel M. Vogt, Florian Haufe, Robert J. Wood, and Conor J. Walsh. Batch Fabrication of Customizable Silicone-Textile Composite Capacitive Strain Sensors for Human Motion Tracking. *Advanced Materials Technologies*, 2(9):1700136, 9 2017.

[3] Ozgur Atalay, Asli Atalay, Joshua Gafford, and Conor Walsh. A Highly Sensitive Capacitive-Based Soft Pressure Sensor Based on a Conductive Fabric and a Microporous Dielectric Layer. *Advanced Materials Technologies*, 3(1):1700237, 1 2018.

[4] Friedrich G Barth. Spider mechanoreceptors. *Current Opinion in Neurobiology*, 14(4):415–422, 8 2004.

[5] Anthony Bond, Brian Mergelas, and Cliff Jones. Pinpointing Leaks in Water Transmission Mains. Technical report, 2004.

[6] Kenneth C Catania. Tactile sensing in specialized predators âĂŞ from behavior to the brain. *Current Opinion in Neurobiology*, 22(2):251–258, 4 2012.

[7] Dimitris M. Chatzigeorgiou. A Reliable & Autonomous Robotic In-Pipe Leak Detection System. 1:1–176, 2015.

[8] Jï£¡rgen Engelberth, Gerhard Wanner, Beate Groth, and ElmarW. Weiler. Functional anatomy of the mechanoreceptor cells in tendrils of Bryonia dioica Jacq. *Planta*, 196(3):539–550, 6 1995.

[9] Wyatt Felt and C. David Remy. Smart braid: Air muscles that measure force and displacement. In *2014 IEEE/RSJ International Conference on Intelligent Robots and Systems*, pages 2821–2826. IEEE, 9 2014.

[10] Amir Firouzeh, Antoine Foba Amon-Junior, and Jamie Paik. Soft piezoresistive sensor model and characterization with varying design parameters. *Sensors and Actuators A: Physical*, 233:158–168, 9 2015.

[11] Osama Hunaidi, Wing Chu, Alex Wang, and Wei Guan. *Leak Detection Methods for Plastic Water Distribution Pipes.* AWWA Research Foundation and american Water Works Association, Ottawa, ON, Canada, 1999.

[12] Osama Hunaidi, Alex Wang, Marc Bracken, Tony Gambino, and Charlie Fricke. Acoustic Methods for Locating Leaks in Municipal Water Pipe Networks. Technical report.

[13] Hu Jin, Erbao Dong, Min Xu, Chunshan Liu, Gursel Alici, and Yang Jie. Soft and smart modular structures actuated by shape memory alloy (SMA) wires as tentacles of soft robots. *Smart Materials and Structures*, 25(8):085026, 8 2016.

[14] Chong-Chan Kim, Hyun-Hee Lee, Kyu Hwan Oh, and Jeong-Yun Sun. Highly stretchable, transparent ionic touch panel. *Science (New York, N.Y.)*, 353(6300):682–7, 8 2016.

[15] Jeonghyun Kim, Giovanni A. Salvatore, Hitoshi Araki, Antonio M. Chiarelli, Zhaoqian Xie, Anthony Banks, Xing Sheng, Yuhao Liu, Jung Woo Lee, Kyung-In Jang, Seung Yun Heo, Kyoungyeon Cho, Hongying Luo, Benjamin Zimmerman, Joonhee Kim, Lingqing Yan, Xue Feng, Sheng Xu, Monica Fabiani, Gabriele Gratton, Yonggang Huang, Ungyu Paik, and John A. Rogers. Battery-free, stretchable optoelectronic systems for wireless optical characterization of the skin. *Science Advances*, 2(8):e1600418, 8 2016.

[16] David W Kurtz. Developments in a Free-Swimming Acoustic Leak Detection System For Water Transmission Pipelines. Technical report, 2006.

[17] Marc-antoine Lacasse and Vincent Duchaine. Characterization of the Electrical Resistance of Carbon-Black-Filled Silicone_Application to a Flexible and Stretchable Robot Skin. 2010.

[18] C. Larson, B. Peele, S. Li, S. Robinson, M. Totaro, L. Beccai, B. Mazzolai, and R. Shepherd. Highly stretchable electroluminescent skin for optical signaling and tactile sensing. *Science*, 351(6277):1071–1074, 3 2016.

[19] Chiara Lucarotti, Massimo Totaro, Ali Sadeghi, Barbara Mazzolai, and Lucia Beccai. Revealing bending and force in a soft body through a plant root inspired approach. 2015.

[20] C Majidi, R Kramer, and R J Wood. A non-differential elastomer curvature sensor for softer-than-skin electronics. *Smart Materials and Structures*, 20(10):105017, 10 2011.

[21] J.M. Muggleton and M.J. Brennan. Leak noise propagation and attenuation in submerged plastic water pipes. *Journal of Sound and Vibration*, 278(3):527–537, 12 2004.

[22] J.M. Muggleton, M.J. Brennan, R.J. Pinnington, and Y. Gao. A novel sensor for measuring the acoustic pressure in buried plastic water pipes. *Journal of Sound and Vibration*, 295(3-5):1085–1098, 8 2006.

[23] Selim Ozel, Nehir A. Keskin, Darien Khea, and Cagdas D. Onal. A precise embedded curvature sensor module for soft-bodied robots. *Sensors and Actuators A: Physical*, 236:349–356, 12 2015.

[24] Rui Pedro Rocha, Pedro Alhais Lopes, Anibal T de Almeida, Mahmoud Tavakoli, and Carmel Majidi. Fabrication and characterization of bending and pressure sensors for a soft prosthetic hand. *Journal of Micromechanics and Microengineering*, 28(3):034001, 3 2018.

[25] Daniela Rus and Michael T. Tolley. Design, fabrication and control of soft robots. *Nature*, 521(7553):467–475, 5 2015.

[26] Mahmoud Tavakoli, Pedro Lopes, Joao Lourenco, Rui Pedro Rocha, Luana Giliberto, Anibal T. de Almeida, and Carmel Majidi. Autonomous Selection of Closing Posture of a Robotic Hand Through Embodied Soft Matter Capacitive Sensors. *IEEE Sensors Journal*, 17(17):5669–5677, 9 2017.

[27] Amy Vickers. The Future of Water Conservation: Challenges Ahead. *Journal of Contemporary Water Research and Education*, 114(1), 7 2011.

[28] Lucie Viry, Alessandro Levi, Massimo Totaro, Alessio Mondini, Virgilio Mattoli, Barbara Mazzolai, and Lucia Beccai. Flexible Three-Axial Force Sensor for Soft and Highly Sensitive Artificial Touch. *Advanced Materials*, 26(17):2659–2664, 5 2014.

[29] Hongbo Wang, Greg de Boer, Junwai Kow, Ali Alazmani, Mazdak Ghajari, Robert Hewson, Peter Culmer, Hongbo Wang, Greg De Boer, Junwai Kow, Ali Alazmani, Mazdak Ghajari, Robert Hewson, and Peter Culmer. Design Methodology for Magnetic Field-Based Soft Tri-Axis Tactile Sensors. *Sensors*, 16(9):1356, 8 2016.

[30] Hongbo Wang, Massimo Totaro, and Lucia Beccai. Toward Perceptive Soft Robots: Progress and Challenges. *Advanced Science*, 5(9):1800541, 9 2018.

[31] Edward L. White, Michelle C. Yuen, Jennifer C. Case, and Rebecca K. Kramer. Low-Cost, Facile, and Scalable Manufacturing of Capacitive Sensors for Soft Systems. *Advanced Materials Technologies*, 2(9):1700072, 9 2017.

[32] You Wu. *Low-cost soft sensors and robots for leak detection in operating water pipes*. PhD thesis, Massachusetts Institute of Technology, 2018.

[33] You Wu, Kristina Kim, Michael Finn Henry, and Kamal Youcef-Toumi. Design of a leak sensor for operating water pipe systems. In *2017 IEEE/RSJ International Conference on Intelligent Robots and Systems (IROS)*, pages 6075–6082. IEEE, 9 2017.

[34] You Wu, Kristina Kim, Michael Finn Henry, and Kamal Youcef-Toumi. Design of a leak sensor for operating water pipe systems. *IEEE International Conference on Intelligent Robots and Systems*, 2017-Septe:6075–6082, 2017.

[35] Dian Yang, Mohit S. Verma, Ju-Hee So, Bobak Mosadegh, Christoph Keplinger, Benjamin Lee, Fatemeh Khashai, Elton Lossner, Zhigang Suo, and George M. Whitesides. Buckling Pneumatic Linear Actuators Inspired by Muscle. *Advanced Materials Technologies*, 1(3):1600055, 6 2016.

[36] Chao Yuan, Devin J. Roach, Conner K. Dunn, Quanyi Mu, Xiao Kuang, Christopher M. Yakacki, T. J. Wang, Kai Yu, and H. Jerry Qi. 3D printed reversible shape changing soft actuators assisted by liquid crystal elastomers. *Soft Matter*, 13(33):5558–5568, 8 2017.

[37] Hao Zeng, Owies M. Wani, Piotr Wasylczyk, and Arri Priimagi. Light-Driven, Caterpillar-Inspired Miniature Inching Robot. *Macromolecular Rapid Communications*, 39(1):1700224, 1 2018.